



저작자표시-비영리-변경금지 2.0 대한민국

이용자는 아래의 조건을 따르는 경우에 한하여 자유롭게

- 이 저작물을 복제, 배포, 전송, 전시, 공연 및 방송할 수 있습니다.

다음과 같은 조건을 따라야 합니다:



저작자표시. 귀하는 원저작자를 표시하여야 합니다.



비영리. 귀하는 이 저작물을 영리 목적으로 이용할 수 없습니다.



변경금지. 귀하는 이 저작물을 개작, 변형 또는 가공할 수 없습니다.

- 귀하는, 이 저작물의 재이용이나 배포의 경우, 이 저작물에 적용된 이용허락조건을 명확하게 나타내어야 합니다.
- 저작권자로부터 별도의 허가를 받으면 이러한 조건들은 적용되지 않습니다.

저작권법에 따른 이용자의 권리는 위의 내용에 의하여 영향을 받지 않습니다.

이것은 [이용허락규약\(Legal Code\)](#)을 이해하기 쉽게 요약한 것입니다.

[Disclaimer](#)

Ph.D. Dissertation

**Phase engineering of
two-dimensional materials for
electronic applications**

August 2022

**Graduate School of Seoul National University
Department of Materials Science and Engineering**

Huije Ryu

Phase engineering of two-dimensional materials for electronic applications

Advisor: Prof. Gwan-Hyoung Lee

by
Huije Ryu

A thesis submitted to the Graduate Faculty of Seoul National University
in partial fulfillment of the requirements
for the Degree of Doctor of Philosophy
Department of Materials Science and Engineering

August 2022

Approved
by

Chair	<u>Ho Won Jang</u>	(Seal)
Vice Chair	<u>Gwan-Hyoung Lee</u>	(Seal)
Examiner	<u>Hyejin Jang</u>	(Seal)
Examiner	<u>Jihyun Kim</u>	(Seal)
Examiner	<u>Jangyup Son</u>	(Seal)

Abstract

Two-dimensional (2D) van der Waals (vdWs) materials, including graphene and transition metal dichalcogenides (TMDs), opened a new research field in future electronics and optoelectronics due to their novel physical, electrical and optical properties. Particularly, 2D materials can be engineered in ultra-scaled dimension to modulate its functionality.

Phase transition is an interesting approach to change properties of 2D materials. To engineering the phase of 2D materials, many strategies have been introduced such as heat, electrostatic doping, tensile strain, plasma treatment, and electric field. From the changed various polymorphs of 2D materials, many practical applications have been demonstrated including monolithic electrical and optical devices, and electrocatalysis. However, since these techniques could induce distortion of layered structure or irregular phase transition, it has been hard to the physics in structural changes of ultrathin layered structures (e.g., layer number and stacking angle dependence). Moreover, there have been a lack of studies on phase and composition changes of 2D materials during heat-mediated phase change process due to their lower thermal stability.

In this thesis, most of works are focused on the phase engineering of 2D materials to tailor their physical properties. Prior to introduce the detailed studies, brief general background about 2D materials including structural modification methods and vdW heterostructures are given in chapter 2. Then, to engineer the structural phase of TMDs, especially Molybdenum dichalcogenide (MoTe_2), analysis on dimensionality and heat distribution of MoTe_2 are described in chapter

3. Because the MoTe_2 has a smaller phase transition barrier energy than other TMDs, I easily transitioned its phase by encapsulation annealing. I observed stepwise increase of phase transition temperature in 2H-to- T_d phase transition of ultrathin MoTe_2 : higher transition temperature for smaller number of layers. From this, I showed that it is possible to precisely control the phase transition of MoTe_2 by using of dimensionality, which enables the demonstration of vertical and lateral phase patterning of MoTe_2 .

Also, I modulated the phase and composition of MoTe_2 in various hBN- MoTe_2 vdW heterostructures by controlling the heat dissipation and evaporation of MoTe_2 . When the vdW heterostructure of hBN-encapsulated MoTe_2 was irradiated by laser, the 2H- MoTe_2 transformed into $1T'$ phase. Meanwhile, MoTe_2 flakes opened to air or covered only one side by hBN transformed into other stoichiometric structures such as Te and Mo_3Te_4 . From these systematic studies, I revealed that control both temperature distribution and evaporation are crucial to engineer the phase of MoTe_2 under laser irradiation.

Finally, I reversibly transitioned phase of MoTe_2 from $1T'$ phase to 2H phase. Laser-induced polycrystalline $1T'$ grain was changed to single-crystalline 2H grain by annealing process. By using in-situ heating transmission electron microscopy (TEM), I studied the propagation mechanism of the $1T'$ -2H phase transition, which revealed that the newly generated 2H-phase is anisotropically and layer-independently propagated. I observed that $1T'$ -to-2H phase fronts travel primarily along the b-axis of the $1T'$ phase with a layer-by-layer phase transformation. Moreover, I observed that the phase transition was initiated at the $1T'$ -2H phase boundaries. The nucleation-less phase transition reduces the energetic barriers for

phase transition, which leads to low-temperature phase transition even at 225 °C. These results describe the microscopic picture of phase transition in MoTe₂, which can be able to expand the same principle on other 2D materials.

Our findings can provide a better understanding of unique properties in phase transition of 2D materials, which can be applied to design a new device based on phase engineering of 2D materials.

Keywords: Two-dimensional materials, Molybdenum Ditelluride (MoTe₂), Hexagonal boron nitride (hBN), Van der Waals heterostructures, Phase transition, 2D Electronics

Student Number: 2019-26834

Table of Contents

Abstract	1
Table of Contents	4
List of Figures	6
Chapter 1. Introduction	13
1.1 Properties of two-dimensionl materials	13
1.2 Synthesis methods of two-dimensionl materials	18
1.3 Phase modulation of two-dimensional materials	21
Chapter 2. Phase transition in two-dimensional materials.....	26
2.1 Dimensionality-driven phase transition of MoTe₂	26
2.1.1 Introduction.....	26
2.1.2 Experimental procedure	27
2.1.3 Results and discussion	
2.1.3.1 Phase transition of MoTe ₂ by encapsulation annealing	32
2.1.3.2 Thickness-dependent phase transition of MoTe ₂	39
2.1.3.3 Phase transition of the artificially-stacked MoTe ₂	48
2.1.4 Conclusions.....	51
2.2 Laser-induced phase transition of MoTe₂.....	53
2.2.1 Introduction.....	53
2.2.2 Experimental procedure	54
2.2.3 Results and discussion	

2.2.3.1 Phase and chemical composition control of MoTe ₂ by laser irradiation and heat dissipation in van der Waals heterostructures ..	56
2.2.3.2 Laser power and layer number dependent phase changes under laser irradiation	64
2.2.3.3 Laser-induced 2H–1T' monolithic heterophase devices.....	66
2.2.4 Conclusions.....	69
2.3 Anisotropic layer-by-layer phase transition of MoTe₂.....	70
2.3.1 Introduction.....	70
2.3.2 Experimental procedure	71
2.3.3 Results and discussion	
2.3.3.1 Phase transition and recovery of MoTe ₂ (2H→1T'→2H phase) via laser irradiation and annealing process	73
2.3.3.2 In-situ electron microscopy measurements for studying the mechanism of anisotropic layer-by-layer phase transition	76
2.3.4 Conclusions.....	82
Chapter 3. Summary	84
References.....	86
Abstract in Korean	96

List of Figures

Chapter 1

Figure 1. (a) Crystal structures of 2D materials. 2D materials can be exfoliated from to bulk crystals, which results from the weak interlayer van der Waals interaction.(1) (b) Periodic table highlighting the elements. General 2D materials consists of these elements.(1) (c) Typical structural configurations of the 2D materials, which are included into eighteen space groups.(12)..... 14

Figure 2. Synthesis strategies of 2D materials. (a and b) Top-down strategies: mechanical (60) and chemical exfoliation of 2D materials from bulk form.(39) (c) Bottom-up growth of 2D materials.(61, 62).....20

Figure 3. (a to c) Atomic structures of 2H, 1T, 1T', and T_d TMDs. Purple and green atoms represent transition metal and chalcogen, respectively21

Figure 4. (a) Periodic table of TMDs, which is mainly organized for transition metal element. Structural phases of each TMDs are summarized with physical properties.(8) (b) Schematic images of the density of states of 1T, 2H, and 3R structures in TMDs.(69).....23

Figure 5. (a) The energy of formula unit MX₂ (M = W, Mo, X= Te, Se) for the 2H, 1T' and 1T phases.(70) (b) Different phases of MoTe₂ and their unique physical properties.(63).....24

Figure 6. Various phase transition strategies of MoTe₂. Chemical intercalation,(80) Physical deformation,(73) Focused energy,(71, 75) Carrier accumulation,(72) and Electric field.(76, 77).....25

Chapter 2

Figure 7. Crystal structures of the 2H and T_d phase MoTe₂ and optical microscopic images of MoTe₂ before and after encapsulation annealing. The insets are the Raman peak intensity maps for the E_{2g} mode of 2H-MoTe₂ and A₁ mode of T_d-MoTe₂.33

Figure 8. (a) Raman spectra of the as-exfoliated and annealed 7L-MoTe₂ at

different temperatures. (b) Polarization-dependent Raman peak intensities of the E_{2g} mode of 2H (235 cm^{-1} , red circles) and A_1 mode of T_d (162 cm^{-1} , green circles). The T_d phase shows the minimum Raman intensity in the two-lobe pattern along the a-axis. (c) Low-frequency polarized Raman spectra of annealed MoTe_2 . When the polarization direction of the incident light is parallel to the a-axis of MoTe_2 , the T_d phase exhibits additional Raman peaks of the A_1 mode at 12 cm^{-1} and splitting of the A_1 peak around 127 cm^{-1} for the alignment of aa due to symmetry breaking, which enables us to distinguish the T_d phase from the $1T'$ phase. 34

Figure 9. (a and b) HAADF-STEM images and corresponding SAED patterns of graphene encapsulated 2H- MoTe_2 (pre-annealing) and T_d - MoTe_2 (post-annealing), respectively. The molybdenum and tellurium atoms are schematically superimposed with the measured interatomic spacings. The red and green dashed lines indicate the crystal symmetries of the 2H and T_d phases, respectively. The other spots originate from the graphene and multiple scattering at the interfaces 35

Figure 10. Atomic structure and polycrystalline structure of transformed T_d - MoTe_2 . (a) Low-magnification cross-section BF- and HAADF-STEM images of hBN/ T_d - MoTe_2 /hBN. (b) Magnified image of cross-section HAADF STEM image. The interface between MoTe_2 and hBN is ultraclean, and there is no atomic diffusion observed after high-temperature annealing. (c) False-color DF-TEM images of T_d - MoTe_2 . (d) SAED pattern of polycrystalline T_d - MoTe_2 in Figure 2c. Polycrystalline T_d - MoTe_2 has only a 60° difference in all of the grains. As single-crystalline 2H- MoTe_2 has threefold armchair directions, armchair direction aligned atomic plane sliding results in a polycrystalline T_d - MoTe_2 that has only a 60° difference in all of the grains. (e) HAADF-STEM image of the 60° glide-reflection GB of polycrystalline T_d - MoTe_2 . (f) HAADF-STEM image of 120° twofold rotation GB. 37

Figure 11. Thickness-dependent phase transition of MoTe_2 . (a and b) Optical microscopic image and corresponding Raman peak intensity map of hBN-encapsulated MoTe_2 with various thicknesses after hBN encapsulation annealing at 995°C . The Raman peak intensity map was obtained from the E_{2g} mode of 2H and A_1 mode of T_d . (c) Schematic illustration of the thickness-dependent phase transition of hBN-encapsulated MoTe_2 . If the T_A is higher than the T_{PT} of thin MoTe_2 ($T_{PT,Thin}$) and lower than that of the thick one ($T_{PT,Thick}$), the phase transition occurs only in the thick region. (d) Phase diagram of the 2H and T_d phases in the hBN-encapsulated MoTe_2 . The red circles indicate that the MoTe_2 exhibited phase transition at the T_A . The T_{PT} substantially increased from 989°C for 7L to 1075°C for 1L as the number of layers decreased. Inset: TPT increasing steps as a function of layer difference. The black dashed curve is a guide to the eye 39

Figure 12. Conceptual diagram about size-dependent phase transition temperature (T_{PT}) distributions in 2D materials and conventional nanocrystals.40

Figure 13. Thermodynamics for thickness-dependent phase transition temperature. (a) Schematic view of nucleation of T_d -MoTe₂ from hBN-encapsulated 2H-MoTe₂. (b) Gibbs free energy difference between 2H- and T_d -MoTe₂ as a function of the nucleus radius. As surface energy effect become more significant in phase transition at reduced thickness, phase transition is more difficult to occur in the thinner MoTe₂, as shown by the larger critical radius of the 2D nucleus (r^*) and larger activation energy for phase transition (ΔG^*). (c) Molar Gibbs energy difference, $G_{T_d} - G_{2H}$, as a function of temperature. G_{T_d} is always smaller than G_{2H} above 987 °C. (d) Surface energy difference between T_d - and 2H-MoTe₂. T_d -MoTe₂ has a higher surface energy than 2H-MoTe₂ for all layer numbers. Inset: the gap of surface energy between 2H and T_d as a function of number of layers. For multi-layered T_d -MoTe₂, the energy difference is almost the same; however, this is not the case for monolayer T_d -MoTe₂.....41

Figure 14. Effects of pressure and charge carrier density on the phase transition of MoTe₂. (a) First-principles calculations for the total energy per unit cell of 2H- and T_d -MoTe₂ as a function of the c -direction lattice parameter. The T_d phase is more stable than the 2H phase below c -direction lattice parameter of around 13 Å. (b) Energy landscape of phase transition under ambient and compressed ($c = 12$ Å) conditions. Charge carrier density was qualitatively described by the Fermi-smearing method ($\sigma =$ Fermi-smearing width). Red- and blue-line circles show non-pressed and compressed conditions, respectively. Under ambient conditions, I observed that the barrier energy for the transition substantially decreases with increasing charge carrier density while the total energy per unit cell of T_d -MoTe₂ decreases slightly. In compressed conditions, albeit the barrier energy is higher than that of the ambient ones, the barrier energy decreases with increasing the charge carrier density.43

Figure 15. Size-dependent phase transition temperature of various nanoparticles and MoTe₂. To illustrate the size-dependent phase transition temperature variation, we normalized the phase transition temperature based on that in a large dimension scale. In general, the smaller nanoparticles show lower T_{PT} , which is contrary to our observation that T_{PT} increases with decreasing number of layers.44

Figure 16. Phase-engineered 2H-MoTe₂/ T_d -MoTe₂ heterophase devices. (a and b) Schematic illustrations and optical microscope images of hBN-encapsulated 2H-MoTe₂ and T_d -MoTe₂ devices with graphene contacts. (c) $I_{DS}-V_{GS}$ characteristics for 2H- and T_d -MoTe₂ channel devices. The 2H-

MoTe₂ device showed an ambipolar semiconducting characteristics, meanwhile T_d-MoTe₂ showed high I_{DS} without gate dependence, which indicates that T_d-MoTe₂ is metallic. (d) I_{DS}-V_{DS} characteristics for 2H- and T_d-MoTe₂ channel devices as a function of back-gate voltage V_{GS} ranging from -60 to 60 V. (e) Schematic representation and optical microscope image of a device with the T_d-2H monolithic heterophase junction in MoTe₂. (f) I_{DS}-V_{GS} characteristics for a monolithic heterophase junction device as a function of back-gate voltage V_{GS} ranging from -60 to 60 V. The device has semiconducting characteristics with a current I_{on}/I_{off} of 10⁶. The inset shows a linear behavior in the I_{DS}-V_{DS} curves, indicating that typical ohmic contact formed at the junction of 2H and T_d.46

Figure 17. Phase transition of the stacked MoTe₂ layers with an inserted monolayer graphene. (a) Phase transition process of the randomly stacked MoTe₂ flakes with an inserted monolayer graphene. The thin and thick 2H-MoTe₂ with different phase transition temperatures are denoted as t-2H and T-2H, respectively. When the stack was annealed at T_{PT,thick} < T_A < T_{PT,thin}, the stacked and thick regions (t-2H/T-2H and T-2H) were changed to the T_d phase, except for the thin region and graphene-inserted region. (b) Optical image and Raman intensity mapping images of annealed monolayer graphene inserted thin MoTe₂/thick MoTe₂ heterostructure. B8MG2MB, B8M2MB, B8MB, and B2MB indicate the areas of hBN/MoTe₂(8L)/Gr/MoTe₂(2L)/hBN, hBN/MoTe₂(8L)/MoTe₂(2L)/hBN, hBN/MoTe₂(8L)/hBN, and hBN/MoTe₂(2L)/hBN. Under annealing at the temperature where B2MB does not change its phase, phase transition occurred at B8MB, B8M2MB, and B8MG2MB.48

Figure 18. (a and b) Selective area electron diffraction patterns in B8M2MB, and B8MG2MB. After annealing, the misaligned stack of 2L and 8L of 2H-MoTe₂ with a twist angle transforms into aligned T_d-MoTe₂ with zero twist angle. (c and d) Schematic illustrations of the crystal orientation rotation of B8M2MB and B8MG2MB. Inserted graphene hindered coupled phase transition phenomena, which could result from increased interface energies for MoTe₂ (2L)/Gr and MoTe₂ (8L)/Gr.50

Figure 19. Laser-induced thermalization of MoTe₂ and heat dissipation in van der Waals heterostructures. (a) Phase diagram of Mo-Te system at atmospheric pressure. (b) Schematic images of various thermodynamically stable phases in the Mo-Te system. (c) Spatial temperature distribution under laser irradiation calculated by finite element method. Since the thermal conductivity of hBN, SiO₂, and air are different, the temperature distribution of MoTe₂ varies depending on the type of material adjacent to MoTe₂. hBN/2H-MoTe₂/hBN, hBN/2H-MoTe₂/SiO₂, 2H-MoTe₂/hBN, and 2H-MoTe₂/SiO₂ are denoted as BMB, BMS, MB, and MS, respectively. (d) The calculated maximum temperature (T_M) in MoTe₂ as a function of laser power. In BMB structure, the T_M reaches the phase transition critical

temperature at 18 mW laser power. Meanwhile, in MB structure, only 11 mW laser power is needed to attain phase transition57

Figure 20. Raman spectra and optical images of MS, MB, BMS, and BMB structures after laser irradiation. (a) Raman spectra of MoTe₂ for 2H-MoTe₂, MS, MB, BMS, and BMB structures. (b-c) Optical images of MS, MB, and BMS structures after laser irradiation. (e) Optical image BMS structures after laser irradiation. Inset: Raman intensity map from A_g mode of 1T' phase and E_{2g} mode of 2H phase59

Figure 21. Plan-view S/TEM images of laser-irradiated stacked structures. (a) TEM image of MS structure after laser irradiation. Inset: diffraction pattern of MS structure. 2H-MoTe₂ and randomly-oriented Te are observed. (b) BF-TEM image and EDS mapping images of Mo and Te of BMS structure. Reorganization of thermally-degraded MoTe₂ generates Te-rich and Mo-rich areas. (c) HAADF-STEM images of Te-rich and Mo-rich area in Figure 21b. Te-rich and Mo-rich areas consist of crystalline Te and Mo₃Te₄. (d) False-color DF-TEM images of laser-irradiated BMB structure. The Laser-irradiated area is transformed from 2H into 1T' phase. 1T'-MoTe₂ is polycrystalline, and grain 1, 2, and 3 have only a 60° crystallographic direction difference because the armchair-direction-aligned atomic slide in pristine 2H-MoTe₂ is energetically favorable. (e) Diffraction patterns of 2H- and 1T'-MoTe₂. The red and green dashed lines indicate the crystal symmetries of 2H and 1T' phases, respectively. The other spots are generated from the graphene and multiple diffraction of electron beam at the interfaces. (f) HAADF-STEM image of the 120° twofold rotation GB and 60° glide-reflection GB in polycrystalline 1T'-MoTe₂. g, HAADF-STEM image of an atomically sharp interface between 2H and 1T' phase.....62

Figure 22. Laser power and layer number dependent phase changes in BMB, MB structures. (a-b) Raman spectra of BMB, MB structure after irradiation of different power of laser. In BMB structure, only laser power of 20.4 mW induced phase transition from 2H to 1T' phase. However, in MB structure, Te defects were generated even at laser power of 9.9 mW. (c) Raman spectra of MoTe₂ as a function of layer numbers in BMB structure. Phase transition is induced in more than 4 layers.64

Figure 23. Device properties of laser-irradiated 2H-1T' monolithic heterophase devices. (a) Schematic images of 1T' channel device with graphene contact. (b) Optical image and Raman peak intensity map images of laser-induced 1T'-MoTe₂ device with graphene contact. Raman peak intensity map images of A_g mode of 1T'-MoTe₂ and G mode of graphene identify the channel and contact area. (c) I_{DS}-V_{GS} curves for 2H- and 1T'-MoTe₂ channel devices. Before laser irradiation, the 2H-MoTe₂ channel device showed ambipolar characteristics. Meanwhile, after irradiation, 1T'-

MoTe₂ channel showed metallic properties. (d) I_{DS}-V_{DS} characteristics for 2H- and 1T'-MoTe₂ channel devices as a function of back-gate voltage V_{GS} ranging from - 60 V to 60 V. (e) Schematic image of 2H-1T' monolithic heterophase device. (f) Optical image and schematic illustration of the 2H-1T' monolithic heterophase device. (g) I_{DS}-V_{GS} characteristics for the 2H-1T' monolithic heterophase device as a function of back-gate voltage V_{GS} ranging from - 3 V to 3 V. The device has semiconducting characteristics with a current I_{on}/I_{off} of 10⁷. (h) I_{DS}-V_{DS} characteristics for the 2H-1T' monolithic heterophase device. Linear behavior of I_{DS}-V_{DS} curves indicates typical Ohmic contact is formed at the junction of 2H and 1T' 66

Figure 24. Characterization of different phases of MoTe₂. (a) Schematic of the reversible phase transition of MoTe₂. Local laser-irradiation induces 2H-to-1T' phase transition of MoTe₂, while the 1T'-MoTe₂ can be reverted back to 2H phase with an annealing process. (b-c) HAADF-STEM images for 2H and 1T' phase, respectively. (d) Raman spectra of 1T'- and 2H-MoTe₂ . 73

Figure 25. Phase and grain orientation mapping of laser-irradiated MoTe₂ with TEM. (a) Bright-field TEM image of the suspended MoTe₂ containing both 2H and 1T' grains. The 1T' phase region was delineated by the laser trajectory and outlined by the black dashed lines. (b-c) Selected-area electron diffraction patterns, (d-e) dark-field TEM images of 2H and 1T' phase, respectively. The diffraction patterns (b-c) are acquired with zone axis perpendicular with the basal planes. The Dark-field TEM images (d-e) are formed by selecting the (-1000) 2H and (-210) 1T' Bragg spots in (b) and (c) with the objective aperture marked with blue and orange circles. (f) Overlay of false-colored Dark-field TEM images of the 2H matrix (red) and three different orientations of 1T' grains (green, yellow, and blue). The Dark-field TEM images (d-f) are acquired at the region marked by the yellow dashed square in (a) 74

Figure 26. Anisotropic 1T'-to-2H phase transition at low temperatures. (a-d) Dark-field TEM images formed from the (-1100) 2H show the 2H phase front propagating from 200 to 275 °C. (e) Overlay of a low magnification dark-field TEM image with newly grown 2H region marked in red. It shows that the 1T'-to-2H phase transition occurs primarily at 2H-1T' interfaces. (f) The contour plot of 2H phase front propagating anisotropically along the b-axis of nearby 1T' grain in the same region as Fig. 3a-d with increasing temperature. The anisotropy arises from the different interface energy of type 1 and 2 interfaces. HAADF-STEM images of (g) type 1 and (h) type 2 2H-1T' interfaces with kinks indicates a step-flow growth model. The propagation rates of interfaces are limited by its kink formation rate. It is much harder to form kinks on coherent type 1 interface, therefore, the growth of type 1 interface along a-axis ([100] 1T') direction is strongly prohibited..... 78

Figure 27. Layer-by-layer phase transition and growth kinetics measurement. (a) Dark-field TEM image that shows the layer-by-layer phase transition. The 2H-1T' interface of different layers is individually identified by their intensity difference. (b) Schematic of the intensity differences of 4-layer MoTe₂ 2H-1T' interfaces in dark-field TEM. The mono-, bi-, tri-, and quad-layer 2H phase fronts are labeled as I, II, III, and IV respectively. Note that the relative heights (in Z-direction) of each phase front remain unknown due to the projection nature of TEM. (c) Plot of 2H phase front positions of different layers as a function of accumulated heating time.....80

Chapter 1. Introduction

1.1. Properties of two-dimensional materials

Structure of two-dimensional materials

Two-dimensional (2D) materials are consisting of layered structures bonded by covalent force in laterally, and each layers are vertically stacked with van der Waals force. Owing to the weak vdW interactions between the layers, atomically thin layers can be isolated from the bulk materials.(2) The lack of surface dangling bonds on 2D materials provides new opportunities for studying unprecedented, dimensionality-driven physical properties in contrast to three dimensional (3D) bulk materials.(3-5) Recent theoretical studies estimate that more than a thousand materials are exfoliable,(6, 7) including the group IV and V crystals (e.g., silicene and phosphorene), transition metal dichalcogenides (TMDs), (e.g., MoS₂, WSe₂), transition metal carbides, and nitrides (e.g., Ti₃C₂T_x, where T = O, OH, F), composite materials of the groups III–V, II–VI, and I–VII (e.g., GaN, hexagonal BN (hBN), and GaAs), and transition metal halides (e.g., CrI₃).*(8-11)* The crystal structure of these 2D materials is classified by many space groups. They belong to 18 space groups such as hexagonal, square, rectangular lattices (Figure 1).*(12)*

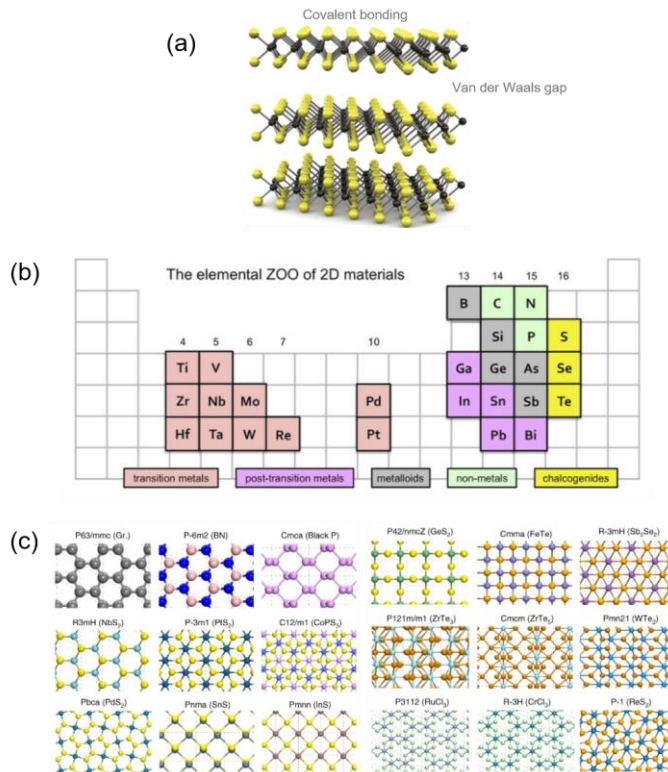


Figure 1. (a) Crystal structures of 2D materials. 2D materials can be exfoliated from to bulk crystals, which results from the weak interlayer van der Waals interaction.(1) (b) Periodic table highlighting the elements. General 2D materials consists of these elements.(1) (c) Typical structural configurations of the 2D materials, which are included into eighteen space groups.(12)

Properties of two-dimensional materials

Due to their distinct electrical, physical, and optical properties, 2D materials; such as graphene; TMDs; hBN; etc., have created a new area of study in the field of low-dimensional materials.

Graphene research has been progressed fast recently since some of its

properties are outperformed to conventional materials. The carrier mobility of graphene reaches $10^6 \text{ cm}^2\text{V}^{-1}\text{s}^{-1}$ at 1.8 K and $10^5 \text{ cm}^2\text{V}^{-1}\text{s}^{-1}$ at room temperature.(13, 14) Also, a graphene monolayer is mechanically strong with a Young's modulus of 1 TPa and intrinsic strength of 130 GPa, which is 5 times larger than steel.(15) It has high thermal conductivity above $3,000 \text{ Wm}^{-1}\text{K}^{-1}$, and superior transparency (97.3% of white light can pass monolayer graphene).(16, 17) Graphene has superior impermeability to any gas molecules even including hydrogen in monolayer thickness.(18)

Due to graphene's zero bandgap, which limits its usage as a semiconductor, research on other 2D materials has taken done. Since TMDs have an initial band gap that is determined by the composition of materials and various structural phases with their polymorphism, TMDs have been emphasized as an appealing candidate for the 2D semiconductor. The monolayer TMDs offer many advantages for scaling the electronic devices over Moore's Law.(19, 20) The transistor fabricated with monolayer MoS_2 shows a good electrical performance without short channel effects, which shows competitive advantage over 3D bulk semiconductors (such as Si or GaAs).(21, 22) Moreover, monolayer TMDs have broken inversion symmetry and the strong spin-orbit coupling, which opens the research field about spin and valley physics.(23) For example, the polarized optical pumping excites spin- and valley-selective excitons in monolayer MoS_2 , which enables simultaneous control over the spin and valley degrees of freedom. TMDs are

promising for optoelectronic applications such as photodetectors and photovoltaic devices, since monolayer TMDs have direct bandgap in the visible frequency range(24) Recently, various exciton complexes were experimentally investigated from monolayer TMDs, which results from the strong Coulomb interaction between electron and hole.(25, 26) Because TMDs are intrinsically highly flexible, films manufactured from these materials are well suited for use as flexible substrates and active layers.(27, 28)

hBN, having hexagonal lattice structure as graphene, is uniquely highlighted by its thermal stability, chemical inertness, and mechanical robustness. hBN has been used for encapsulating other 2D materials due to its thermal stability and chemical inertness. Compared with the traditional substrates, hBN has atomically flat surface without dangling bonds and surface charge traps.(29) Moreover, hBN has the large bandgap (5.8 eV), high breakdown field (8 MV/cm), outstanding thermal conductivity, and high surface optical phonon energy (two times higher than that of SiO₂), which makes hBN suitable in gate dielectric and substrate for other 2D materials. For example, hBN substrate provide both the reduced roughness and charge impurity, which enables the ballistic conduction of graphene channel, with an electronic mean free path of few tens of micrometer. The hBN-encapsulated graphene device shows intrinsic carrier mobility of graphene (10^6 cm²/Vs at $n = 10^{12}$ cm⁻²). (30) In addition, hBN-encapsulated TMDs show its intrinsic

electronic, optical properties, which results from the suppression of inhomogeneous broadening arising from external environment, such as substrates and adsorbents. For example, hBN-encapsulated WS₂ shows reduced photoluminescence peak whose full-width at half-maximum (FWHM) of ~26 meV in contrast to WS₂ on a silicon substrate shows ~75 meV.(31-33) Recent research of hBN focuses on a unique photonic properties of hBN. Defect-engineered hBN shows single-photon emission, which exhibits second-order nonlinearities.(34) And the large band gap of hBN enables to emit and detect the light in deep UV range.(35, 36)

1.2. Synthesis methods of two-dimensional materials

Top-down strategy

Since monolayer graphene was mechanically peeled from bulk graphite,(37, 38) exfoliation techniques have been one of the most feasible methods to obtain high-quality 2D materials. As the interlayer bonding energy between each layer in vdW materials is weak, various external forces can isolate 2D materials from vdW bulk crystals.

Mechanical exfoliation (that is, the so-called Scotch tape method) is an typical method to produce 2D materials in laboratory scale. However, it has limits in enlarging the size of flakes or controlling the layer number of 2D materials. Meanwhile, metal films have strong affinity to many 2D materials, which makes the uniform bond between metal and vdW bulk crystal.(12) Using metal substrates or directly evaporated metal films, large size of monolayer 2D materials can be exfoliated with lateral dimensions even on the cm scale (Figure 2a).(39, 40)

For large-scale preparation of monolayer 2D materials, intercalation-based liquid exfoliation has been widely used.(41) Intercalation of molecules (or ion) can expand the interlayer spacing. Chemical intercalation expands two adjacent layers, which weakens the van der Waals force, leading to decrease of interlayer binding energy. The intercalated bulk 2D materials can be exfoliated more easily.(42) Compared with mechanical exfoliation, this

technique is more productive. However, it is hard to get large size flakes with high crystallinity. In addition, the chemical treatments sometimes induce modified chemical or physical properties of 2D materials (Figure 2b).

Bottom-up strategy

To solve the issues for the large-scale preparation, the researchers focused on the synthesis of 2D materials with chemical vapor deposition (CVD)(43-54). Gas phase precursors under a controlled atmosphere are supplied to heated substrate, the condensed precursor element forms 2D materials. CVD is a simple method for manufacturing 2D materials, but it does not always grantee the uniform growth of 2D materials due to inhomogeneous gas flow and temperature gradient of substrate. In metal-organic CVD (MOCVD), metal-organic sources are pyrolyzed on the target substrate for the growth of 2D materials.(55, 56) The high purity of the reactants allows for high homogeneity, and the growth scale is determined by reactor setups, which can be made large enough to synthesis wafer scale 2D materials. Through MOCVD, large-scale growth of 2D materials is possible at low temperatures, it usually requires significantly longer time (> 12 h). Substrate interactions with 2D materials are important to the properties of grown 2D materials. Strain, symmetry and chemical interactions are mainly affect the properties of grown 2D materials.(57-59) Interestingly, grown 2D materials and 2D substrates could have epitaxial relation despite of weakly

interacting without dangling bonds in 2D substates, which is called to van der Waals epitaxy. The weak van der Waals interaction leads to reduced constraints to matching of lattice structure and symmetry (Figure 2c).

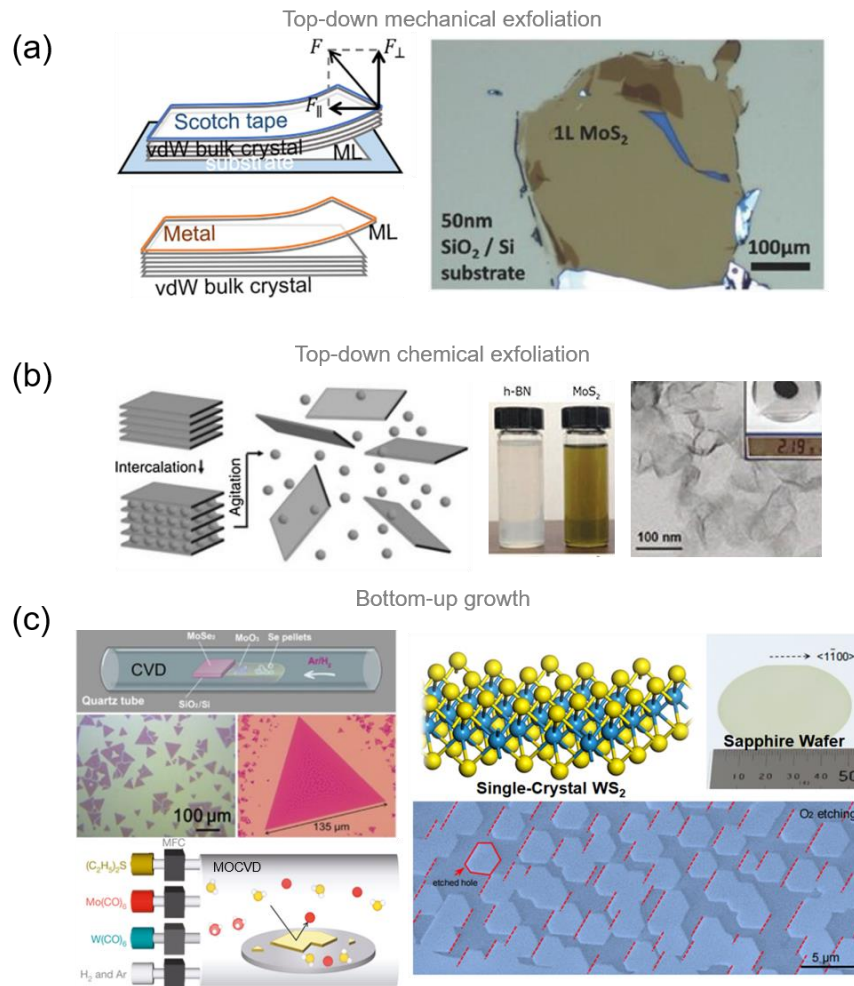


Figure 2. Synthesis strategies of 2D materials. (a and b) Top-down strategies: mechanical (60) and chemical exfoliation of 2D materials from bulk form.(39) (c) Bottom-up growth of 2D materials.(61, 62)

1.3. Phase modulation of two-dimensional materials

Polymorphism in 2D materials

Among 2D materials, TMDs have been studied especially for its phase transition behaviors. Phase of TMDs are included into five lattice structures: hexagonal (2H); octahedral (1T); distorted octahedral (monoclinic) (1T'); rhombohedral (3R); and orthorhombic (T_d), and each phase has their own electrical and optical properties; (Figure 3).(63)

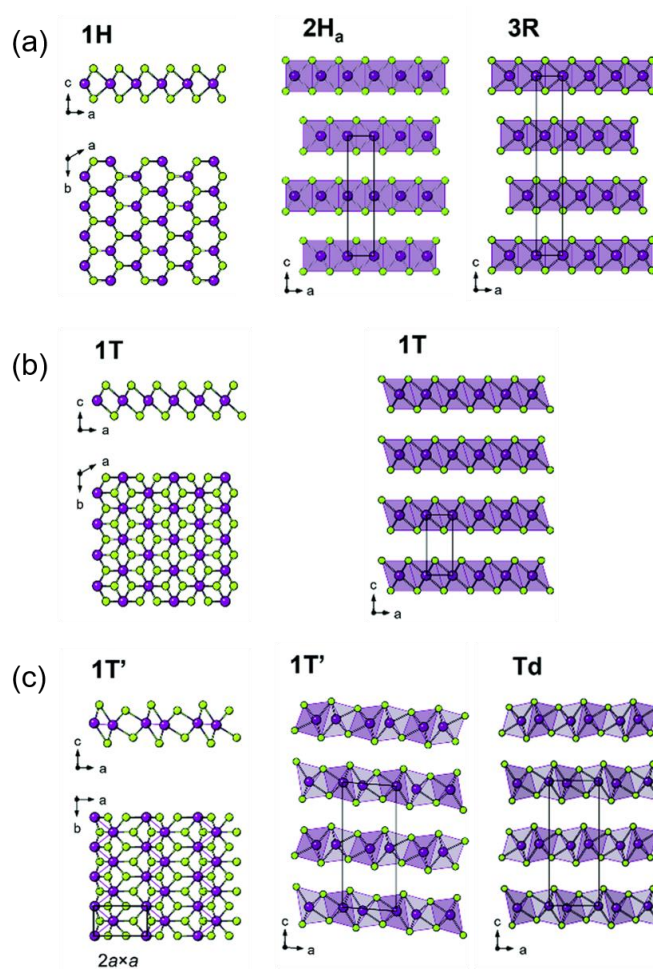


Figure 3. (a to c) Atomic structures of 2H, 1T, 1T', and T_d TMDs. Purple and green atoms represent transition metal and chalcogen, respectively.(64)

Since the atomic and electronic structures have strong correlation, these polymorphs exhibit distinct electrical properties (Figure 4). In TMDs, the energy of chalcogen p orbitals are located at lower than the Fermi level. Therefore, the electrical properties of TMDs are determined by the filling of d orbitals of transition metal. For the 2H phase having hexagonal symmetry, the *d* orbitals are made up of d_{z^2} ; $d_{x^2-y^2,xy}$; and $d_{xy,yz}$ orbitals, which generating band gap between the d_{z^2} and $d_{x^2-y^2,xy}$ orbitals. In contrast, for the 1T phase with tetragonal symmetry, the $d_{xy,yz,zx}$ and $d_{x^2y^2,z^2}$ orbitals compose the *d* orbitals. *d* orbitals are partially filled, leading to the metallic properties of 1T, 1T', and T_d phases (Figure 4b). Moreover, these specific electronic structures for various polymorphs induce the exotic quantum states including Weyl semimetal states, superconductivity, anisotropic spin-orbit coupling, and quantum spin Hall states.(65-68)

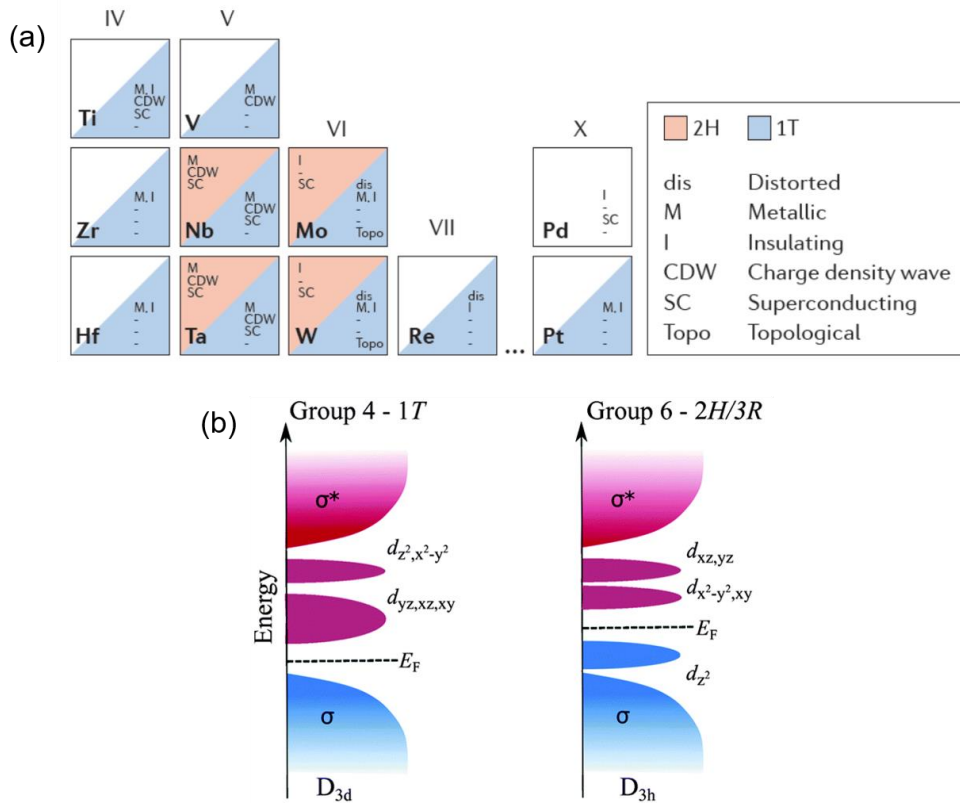


Figure 4. (a) Periodic table of TMDs, which is mainly organized for transition metal element. Structural phases of each TMDs are summarized with physical properties.(8) (b) Schematic images of the density of states of 1T, 2H, and 3R structures in TMDs.(69)

Phase transition in $MoTe_2$

Among TMDs, $MoTe_2$ can be stably existed as semiconducting 2H and semimetallic 1T(T_d) phases in atmosphere condition, due to small energy difference (~ 35 meV) between each phases (Figure 5a). These phases show distinct electrical(optical) properties (Figure 5b).

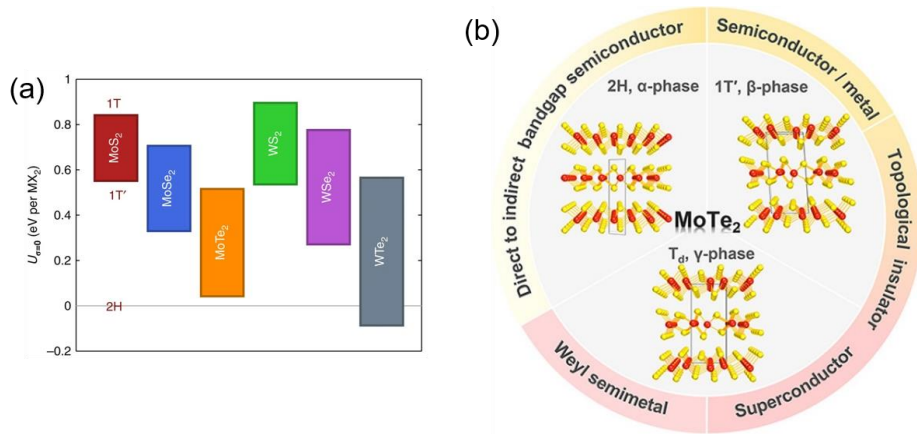


Figure 5. (a) The energy of formula unit MX_2 ($M = W, Mo, X = Te, Se$) for the 2H, 1T' and 1T phases.⁽⁷⁰⁾ (b) Different phases of $MoTe_2$ and their unique physical properties.⁽⁶³⁾

So far, many of phase transition methods for $MoTe_2$ have been reported such as electrostatic doping, electric field, terahertz light field, electron beam irradiation, laser irradiation, and tensile strain ⁽⁷¹⁻⁷⁸⁾ (Figure 6). These developments offer a huge potential for application in novel concepts and functional devices, including strain sensors,⁽⁷⁹⁾ phase-change memories,⁽⁷⁶⁾ and high-performance field-effect transistors with low contact resistance.⁽⁷¹⁾

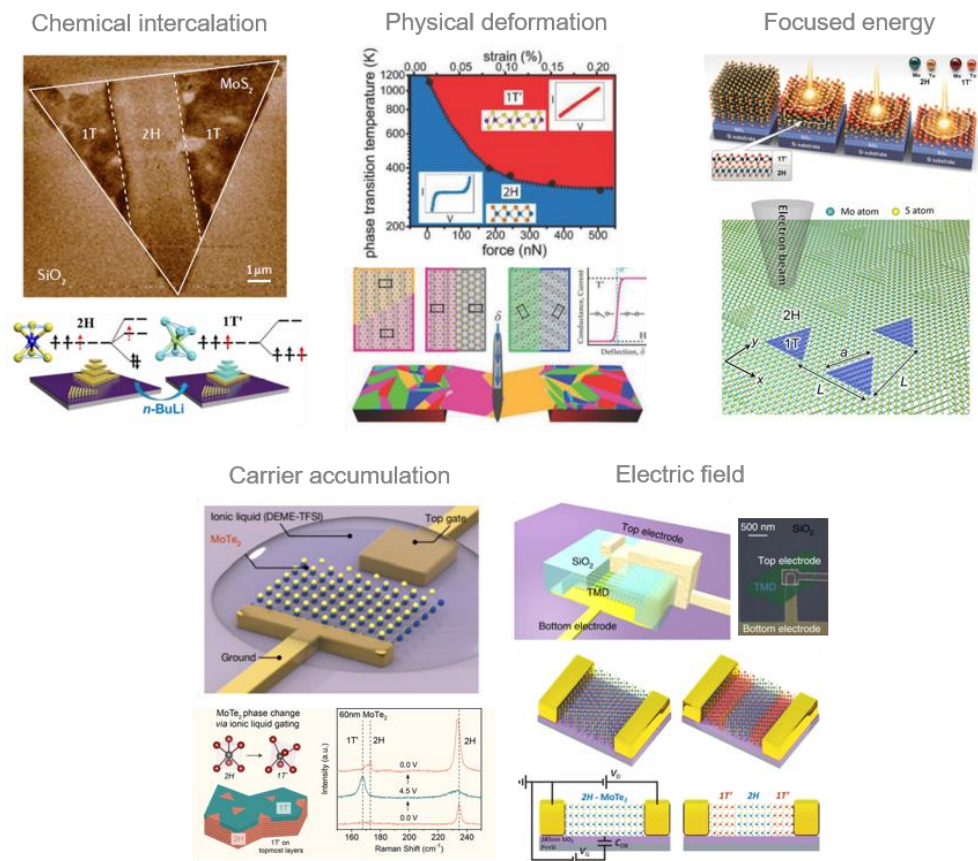


Figure 6. Various phase transition strategies of MoTe₂. Chemical intercalation,(80) Physical deformation,(73) Focused energy,(71, 75) Carrier accumulation,(72) and Electric field.(76, 77)

The small phase transition energy barrier between 1T' and 2H phases enables a unique phase-transition-assisted lateral epitaxial growth, leading to produce the wafer-scale semiconducting single crystal MoTe₂.(81)

Chapter 2. Phase transition in two-dimensional materials

2.1. Dimensionality-driven phase transition of MoTe₂

This chapter has been published in journal. Manuscript are reproduced with permission from Ryu et al., *Adv. Func. Mater.* **31**, 2107376 (2021). Copyright 2022 Wiley-VCH GmbH.(115)

2.1.1 Introduction

As wide range of applications have needed scale down of materials, a precise control of phase in nanoscale has been more significant. When the size of materials decreases, the large surface-to-volume ratio dramatically changes the phase transition behaviors, leading to stabilize phases under conditions in which they are normally not stable at bulk.(82-84) Since the increase of surface-to-volume ratio becomes steeper as the materials size down to a few nm scales, the dimensionality control of nanomaterial is important to modulate the phase of it. However, the atomically-precise design of dimensionality in three-dimensional (3D) nanocrystal is hindered from the limited size controllability and surface reconstruction.(85-87)

2D materials including layered structure with stacked through the van

der Waals interaction, for example, graphene, TMDs have been recognized as a promising functional material that can be engineered in atomically-precise limit. Particularly, MoTe₂ have been studied as a promising phase-changeable material. So far, various phase transition strategies for MoTe₂ have been introduced in previous studies such as laser irradiation⁽⁷¹⁾, electrostatic doping,⁽⁷²⁾ tensile strain,⁽⁷³⁾ plasma treatment,⁽⁷⁴⁾ electron beam irradiation,⁽⁷⁵⁾ electric field,^(76, 77) and terahertz light field.⁽⁷⁸⁾ However, since these methods accompany deformation of layer structure or incomplete phase transition, there has been a few researches on the dimensionality (thickness and stacked heterostructure)-dependence of phase transition in 2D materials.

Here, I report the anomalous dimensionality-driven phase transition of MoTe₂ by hBN-encapsulation annealing. Single crystal few-layer 2H-MoTe₂ transformed into polycrystalline T_d-MoTe₂ with well-stitched grain boundaries. I observed a thickness-dependent transition temperature where the thinner MoTe₂ had a higher transition temperature. I also demonstrate that the vertical and lateral phase transitions of the stacked MoTe₂ flakes can be controlled by inserted graphene layers and the thickness of the heterostructure.

2.1.2 Experimental procedure

Stacking process and encapsulation annealing

All 2D flakes used for fabrication were mechanically exfoliated onto SiO₂/Si substrates. The thickness of each material was separately confirmed using a combination of AFM and optical contrast. To encapsulate MoTe₂ between hBN, I used the pick-up transfer technique with a polypropylene carbonate (bisphenol A carbonate, Sigma Aldrich) (PC)-coated poly (dimethyl siloxane) (PDMS) lens mounted on a slide glass to pick-up and release.⁽³⁰⁾ The PDMS/PC/slide glass was held in a 3-axis micromanipulator to control the position of the contact area. By only controlling the temperature of the stage (80–130 °C), the top hBN was picked up completely by the PC without cracking or folding. After detaching hBN from the substrates, MoTe₂ and the bottom hBN were picked-up by van der Waals forces from the top hBN to form hBN/MoTe₂/hBN ultrathin 2D heterostructures. Note that MoTe₂ must be fully encapsulated by hBN without bubbles. Otherwise, MoTe₂ is degraded during the annealing process. After stacking, the heterostructure was transferred onto a clean SiO₂/Si substrate by releasing the PC film from the PDMS lens at a temperature above 180 °C. Finally, in order to remove the PC film, I placed the samples in chloroform for 30 min. For the phase transition of MoTe₂, the sandwiched MoTe₂ was annealed in a vacuum of 10⁻⁴ Torr. The furnace temperature was ramped up to the target annealing temperature for 3 hours and maintained for 3 hours. Then, the furnace was naturally cooled to room temperature.

Raman spectroscopy

The Raman spectra were acquired using Raman spectroscopy (Renishaw) with a 532 nm laser. To minimize damage of the sample by irradiation of the laser, a power of < 5 mW was used with an acquisition time of 60 s. Since laser spot size is about 1 μm , mapping area was scanned with 1 μm point-to-point distance. All measurements were conducted at room temperature after cooling down the annealed samples. The linearly polarized Raman measurements were carried out in the backscattering geometry using 514.5 nm laser excitation. The input laser beam was focused onto the samples by a 40 \times microscope objective lens (0.6 NA), and the scattered light was collected and collimated by the same objective lens. To access the low-frequency range below 50 cm^{-1} , volume holographic filters (Optigrate) were used to clean the laser lines and reject the Rayleigh-scattered light. A laser with a power below 200 μW was used to avoid local heating. The Raman scattering signals were dispersed by a Jobin–Yvon iHR550 spectrometer with a 2400 grooves/mm grating (400 nm blaze) and detected by a liquid-nitrogen-cooled back-illuminated charge-couple-device (CCD) detector. An achromatic half-wave plate was used to rotate the polarization of the linearly polarized laser beam to the desired direction. The analyzer angle was set such that photons with polarization parallel to the incident polarization passed through. Another achromatic half-wave plate was placed in front of the spectrometer to keep the polarization direction of the signal entering the

spectrometer constant with respect to the groove direction of the grating. The crystal orientation of T_d - MoTe_2 was identified using an anisotropic polarized Raman response.

Transmission electron microscopy

I acquired TEM and HAADF-STEM images to confirm the crystal structure and crystallographic orientations of T_d - MoTe_2 . TEM samples were prepared using the poly (methyl methacrylate) (PMMA)-based transfer method. Samples on PMMA film were transferred to holey Si_3N_4 TEM grids (TED PELLA, 21581-10) and Si_3N_4 nanofilm TEM grids (TEM Windows, SN100-A10Q33B). Then, I removed the PMMA film by placing the samples in acetone for 12 h. Bright-/dark-field TEM images and SAED patterns were acquired using the JEOL-2100Plus at operating voltage of 200 kV. DF-TEM images were taken using an objective aperture with a 1.22 nm^{-1} diameter for acquisition time of 5 s. A double-Cs-aberration-corrected JEOL ARM-200F was used for HAADF-STEM images at operating voltage of 80 kV with a 23 mrad convergence angle and collection semi-angles from 68 to 280 mrad. Cross-section TEM samples were prepared by evaporating a 10 nm protective layer of amorphous carbon on top of the heterostructure, followed by using standard focused ion beam lift-out procedures in a FEI Helios 600i Dual Beam FIB-SEM. Final milling was performed at 2 kV with a cryo-finger inserted to minimize damage and redeposition. Samples were imaged in a

Thermo Fisher Scientific Themis-Z aberration-corrected STEM operated at 80 kV with a 25 mrad convergence angle.

First-principles calculations

To investigate the phase transition of bulk MoTe₂ between 2H and T_d, I performed *ab initio* calculations as implemented in the VASP code.(88, 89) Projector augmented wave potentials(88, 89) were employed to describe the valence electrons, and the electronic wave functions were expanded by a plane wave basis set with a cutoff energy of 450 eV, and the atomic relaxation was continued until the Hellmann–Feynman force acting on every atom was lower than 0.005 eV/Å. For the exchange correlation functional, I used the rev-vdW-DF2 method,(90) which is known to be suitable for computing atomic structures of layered TMDs. The BZ was sampled using a 16 × 32 × 8 k-grid for the primitive unit cells. All parameters have been thoroughly tested to describe the structures and energies of the 1T' MoTe₂ single layer. To simulate the pressure effect with the hBN encapsulation, I adjust the lattice parameter along the c-direction for a given pressure accordingly. To simulate the effect of charge carrier generation at a finite temperature, I used the Fermi–Dirac smearing method as was used in the other study.(78)

Device fabrication and electrical measurement

E-beam lithography was performed to develop patterns of metal pads

and create a via-contact for graphene electrodes encapsulated by hBN. The van der Waals heterostructure was etched by exposing the pre-patterned structure to XeF_2 .⁽⁹¹⁾ The top hBN was etched away, and the embedded graphene electrodes stopped the etching process. Metals of Cr/Pd/Au (1 nm/30 nm/40 nm) were then deposited on the exposed graphene electrodes using an e-beam evaporator. Finally, a lift-off process was performed on the samples by soaking them in acetone. The electrical measurements of the devices were conducted using a parameter analyzer (Keithley 2400) at room temperature under ambient conditions.

2.1.3 Results and discussions

2.1.3.1 Phase transition of MoTe_2 by encapsulation annealing

To investigate the phase transition of MoTe_2 , I used encapsulation annealing using hBN. To prevent evaporation of MoTe_2 during annealing, stacks of hBN/ MoTe_2 /hBN were fabricated by the pick-up technique, where hBN flakes with a thickness of ~ 10 nm were used. The stacks were annealed at 980–1080 °C in a vacuum. Figure 7 shows optical images of hBN-encapsulated MoTe_2 flakes of 4 layers and 7 layers before and after annealing, where the 7L- MoTe_2 was fully encapsulated and 4L- MoTe_2 was partially encapsulated. Although the un-covered 4L- MoTe_2 evaporated entirely, the

fully encapsulated 7L-MoTe₂ was preserved after annealing at 1000 °C, which indicates that fully encapsulated MoTe₂ within the hBN is highly stable at high temperatures because of the stability and impermeability of hBN.

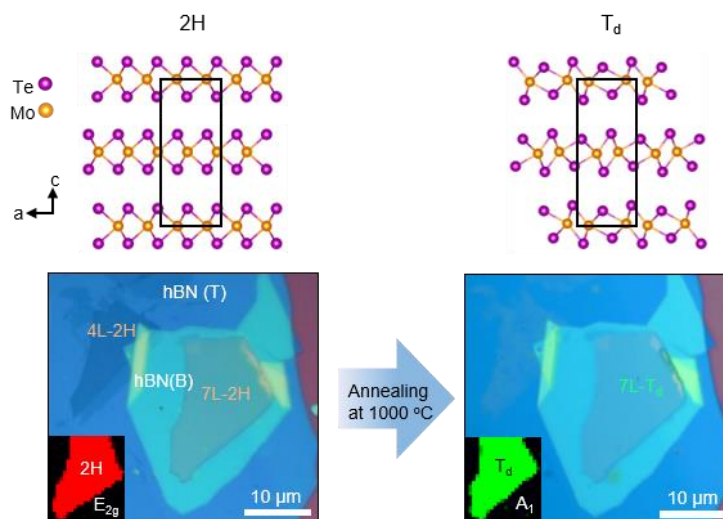


Figure 7. Crystal structures of the 2H and T_d phase MoTe₂ and optical microscopic images of MoTe₂ before and after encapsulation annealing. The insets are the Raman peak intensity maps for the E_{2g} mode of 2H-MoTe₂ and A₁ mode of T_d-MoTe₂.

The Raman spectra of the encapsulation-annealed 7L MoTe₂ at different annealing temperatures (T_A) were measured with a 532 nm laser (Figure 8). When the hBN-encapsulated MoTe₂ was annealed at 800 and 900 °C, the three typical Raman peaks (E_{2g}, A_{1g}, and B_{2g}) of the 2H phase were maintained.⁽⁹²⁾ However, the annealed MoTe₂ at 1000 °C only exhibited the Raman peaks of the A₁ and A₂ modes of the T_d phase, as indicated by filled and empty square boxes, respectively. To verify the formation of the T_d phase,

linear polarized Raman spectroscopy was used in a low-frequency range (Figure 8c).(93, 94) The upper and lower insets in Figure 1b show the Raman peak intensity maps for E_{2g} of 2H and A_1 of T_d , respectively. This indicates that 2H-MoTe₂ uniformly transformed into the T_d phase.

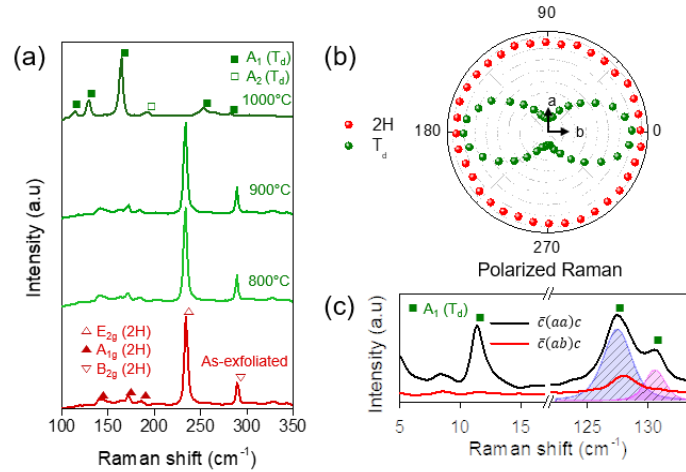


Figure 8. (a) Raman spectra of the as-exfoliated and annealed 7L-MoTe₂ at different temperatures. (b) Polarization-dependent Raman peak intensities of the E_{2g} mode of 2H (235 cm^{-1} , red circles) and A_1 mode of T_d (162 cm^{-1} , green circles). The T_d phase shows the minimum Raman intensity in the two-lobe pattern along the a-axis. (c) Low-frequency polarized Raman spectra of annealed MoTe₂. When the polarization direction of the incident light is parallel to the a-axis of MoTe₂, the T_d phase exhibits additional Raman peaks of the A_1 mode at 12 cm^{-1} and splitting of the A_1 peak around 127 cm^{-1} for the alignment of aa due to symmetry breaking, which enables us to distinguish the T_d phase from the $1T'$ phase.

To investigate the crystal structures of MoTe_2 with high-angle annular dark-field scanning transmission electron microscopy (HAADF-STEM), I developed a method to prepare plan-view TEM samples using the graphene etch stop technique.⁽⁹¹⁾ I fabricated a stack of hBN/Gr/ MoTe_2 /Gr/hBN by encapsulating MoTe_2 with monolayer graphene and hBN. After annealing, the thick hBN layers were removed by XeF_2 exposure, leaving graphene-encapsulated MoTe_2 . In the graphene-encapsulated samples, I can clearly observe the atomic resolution structure of MoTe_2 because of the low atomic number of the carbon atoms.⁽⁹⁵⁾ Figures 9, a and b show the HAADF-STEM images and corresponding selected area electron diffraction (SAED) patterns of 2H- and T_d - MoTe_2 . As the $1T'$ and T_d phases have different stacking configurations, as shown by the atomic models in Figure 7, each phase can be distinguished from out-of-plane HAADF-STEM images.⁽⁶⁷⁾ The well-resolved atom position in Figure 9 clearly shows that the annealed MoTe_2 is a highly crystalline T_d phase with no lattice distortion or massive atomic loss. The d-spacings of the T_d phase calculated from the SAED pattern are well matched with those in previous studies.^(72, 75)

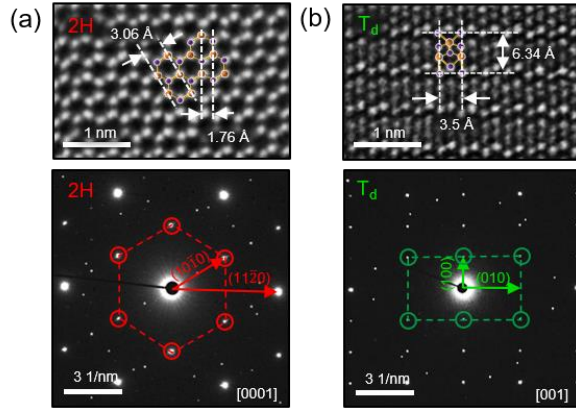


Figure 9. (a and b) HAADF-STEM images and corresponding SAED patterns of graphene encapsulated 2H-MoTe₂ (pre-annealing) and T_d-MoTe₂ (post-annealing), respectively. The molybdenum and tellurium atoms are schematically superimposed with the measured interatomic spacings. The red and green dashed lines indicate the crystal symmetries of the 2H and T_d phases, respectively. The other spots originate from the graphene and multiple scattering at the interfaces.

Figure 10 shows the bright-field and HAADF cross-section STEM images of the 8L-MoTe₂ annealed at 1000 °C. The interfaces between hBN and MoTe₂ are atomically sharp and clean even after annealing. The magnified DF-STEM image in Figure 10b shows that the T_d phase formed without any damage or interlayer diffusion. The false-color dark-field transmission electron microscopy (DF-TEM) image in Figure 10c (obtained from the electron diffraction pattern in Figure 10d) shows that the transformed T_d-MoTe₂ consists of multiple micrometer-sized grains well-stitched along

the straight grain boundaries (GBs), which is in agreement with theoretical prediction.⁽⁹⁶⁾ T_d - MoTe_2 forms unique polycrystalline structure of polygonal grains and sharp GBs to reduce the interface energy of the GBs with misfit strain by the Wulff construction. The different colors of grains in the DF-TEM image were determined from three selected spots of the electron diffraction pattern. The three selected patterns have only an angle difference of 60° . The crystal structure of $2H$ - MoTe_2 is three-fold symmetric; as a result, glide of atomic planes along the three different armchair directions of $2H$ - MoTe_2 produces polycrystalline T_d - MoTe_2 , which has only a 60° difference in all grain.⁽⁷⁵⁾

I performed first-principles calculations to find out the optimal atomic configurations of GBs in polycrystalline T_d - MoTe_2 . As consistent with an earlier study on GBs in a single layer MoTe_2 ,⁽⁹⁶⁾ our multilayers also show that the $[010]$ directions of contiguous grains at the GBs have angles of 60° or 120° as shown in Figures 10, e and f.

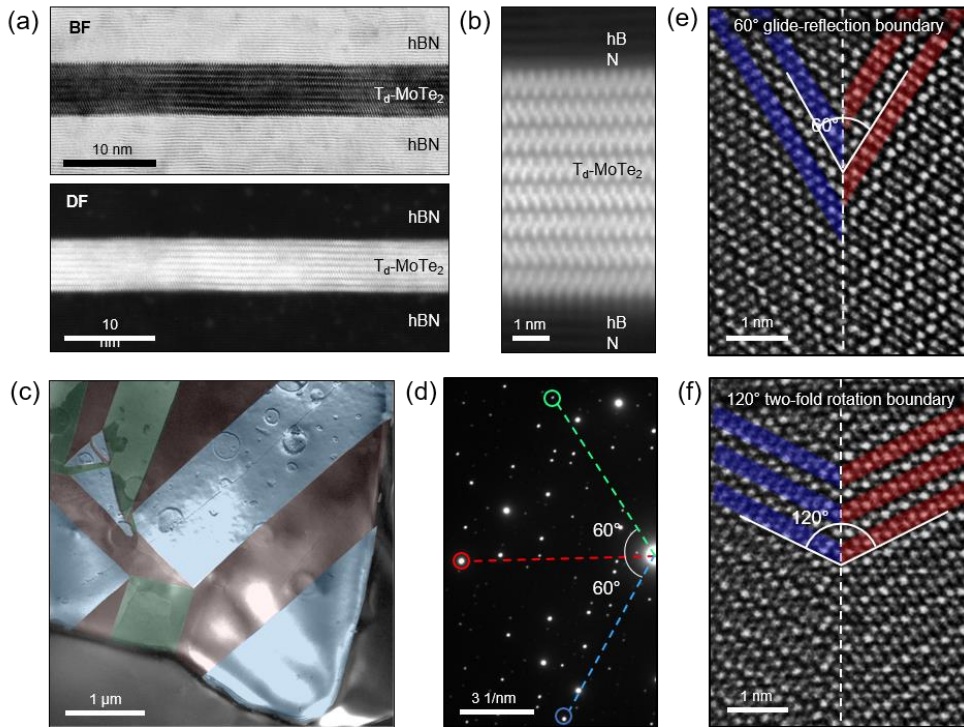


Figure 10. Atomic structure and polycrystalline structure of transformed T_d - MoTe_2 . (a) Low-magnification cross-section BF- and HAADF-STEM images of hBN/ T_d - MoTe_2 /hBN. (b) Magnified image of cross-section HAADF STEM image. The interface between MoTe_2 and hBN is ultraclean, and there is no atomic diffusion observed after high-temperature annealing. (c) False-color DF-TEM images of T_d - MoTe_2 . (d) SAED pattern of polycrystalline T_d - MoTe_2 in Figure 2c. Polycrystalline T_d - MoTe_2 has only a 60° difference in all of the grains. As single-crystalline 2H- MoTe_2 has threefold armchair directions, armchair direction aligned atomic plane sliding results in a polycrystalline T_d - MoTe_2 that has only a 60° difference in all of the grains. (e) HAADF-STEM image of the 60° glide-reflection GB of polycrystalline T_d - MoTe_2 . (f) HAADF-STEM image of 120° twofold rotation GB.

3.1.3.2 Thickness-dependent phase transition of MoTe₂

I observed that the phase transition temperature (T_{PT}) of hBN-encapsulated MoTe₂ increases with a decreasing number of layers. When the MoTe₂ flake with regions of different thicknesses were annealed at 995 °C, the thicker regions underwent a 2H-to- T_d transition, while the 2L region remained in the 2H phase, as shown in the optical images and corresponding Raman intensity map of Figures 11, a and b. The schematic of Figure 11c shows that the phase of MoTe₂ can be spatially defined by a thickness-dependent phase transition. By encapsulating a number of samples with different thicknesses, constructed a phase diagram of MoTe₂, as shown in Figure 11d. As the number of layers decreases, T_{PT} increases in steps. It should be noted that the transition temperature gaps increase from 1 °C for 6-7L to 77 °C for 1-2L as shown in the inset of Figure 11d.

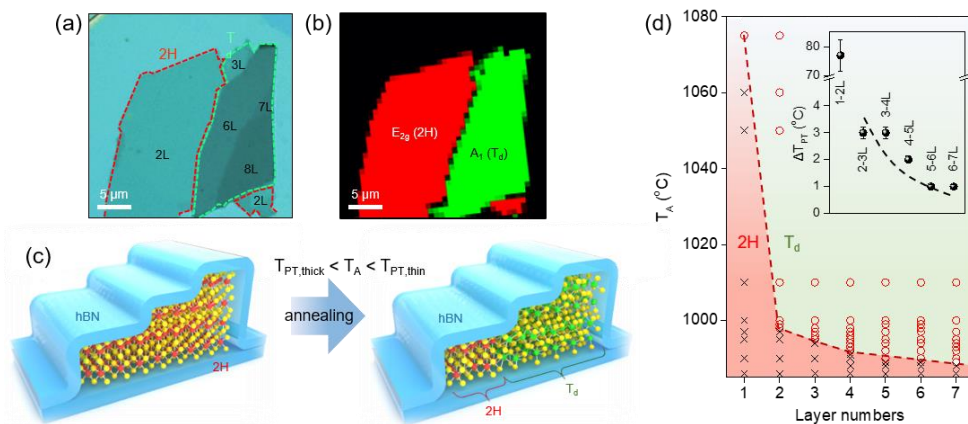


Figure 11. Thickness-dependent phase transition of MoTe₂. (a and b) Optical

microscopic image and corresponding Raman peak intensity map of hBN-encapsulated MoTe₂ with various thicknesses after hBN encapsulation annealing at 995 °C. The Raman peak intensity map was obtained from the E_{2g} mode of 2H and A₁ mode of T_d. (c) Schematic illustration of the thickness-dependent phase transition of hBN-encapsulated MoTe₂. If the T_A is higher than the T_{PT} of thin MoTe₂ (T_{PT,Thin}) and lower than that of the thick one (T_{PT,Thick}), the phase transition occurs only in the thick region. (d) Phase diagram of the 2H and T_d phases in the hBN-encapsulated MoTe₂. The red circles indicate that the MoTe₂ exhibited phase transition at the T_A. The T_{PT} substantially increased from 989 °C for 7L to 1075 °C for 1L as the number of layers decreased. Inset: TPT increasing steps as a function of layer difference. The black dashed curve is a guide to the eye.

The large transition temperature difference in a few atom-thick range enables precise control of the phase transition in ultrathin layered materials. As described in Figures 12, a and a, the conventional nanoparticles with a broad size distribution around b₁ and b₂ have a large overlap in the phase transition temperature ranges around T_{PT,b1} and T_{PT,b2} so that it is difficult to selectively induce phase transition for the desired nanoparticles with specific size. However, the MoTe₂ sheets with discrete thickness difference (a₁ and a₂) of atomically defined distribution have distinct phase transition temperatures of T_{PT,a1} and T_{PT,a2}, which enables precise control of phase transition by

thickness of MoTe₂.

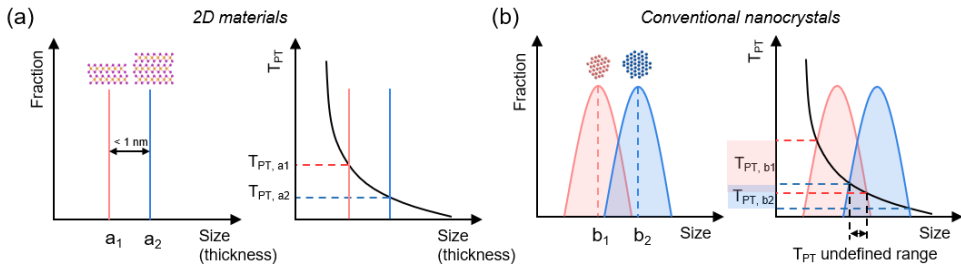


Figure 12. Conceptual diagram about size-dependent phase transition temperature (T_{PT}) distributions in 2D materials and conventional nanocrystals.

The increase of T_{PT} with decreasing thickness of MoTe₂ is due to the significant contribution of the surface energy in the nucleation and growth of the newly formed phase. To clarify this, I assumed a model which has a thin cylindrical disc-type nucleus (Figure 13a). The calculated bulk energy of T_d is smaller than that of 2H over the transition temperature (Figure 13c). Therefore, an inverse relation between T_{PT} and thickness indicates that T_d should have a larger surface energy than 2H. As a result, thinner MoTe₂ requires a larger critical radius of the 2D nucleus (r^*) and larger activation Gibbs free energy (ΔG^*) for the growth of T_d (Figure 13b). As predicted, I revealed that the surface energy of T_d phase is larger than that of the 2H phase by calculating the surface energies from the transition temperatures of Figure 13d.

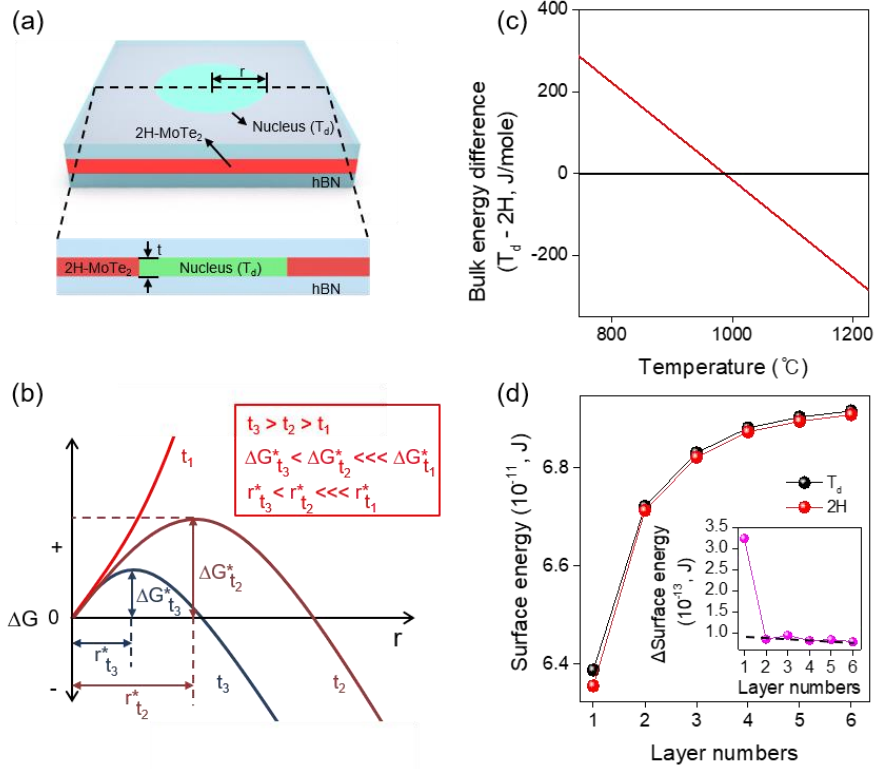


Figure 13. Thermodynamics for thickness-dependent phase transition temperature. (a) Schematic view of nucleation of T_d-MoTe₂ from hBN-encapsulated 2H-MoTe₂. (b) Gibbs free energy difference between 2H- and T_d-MoTe₂ as a function of the nucleus radius. As surface energy effect become more significant in phase transition at reduced thickness, phase transition is more difficult to occur in the thinner MoTe₂, as shown by the larger critical radius of the 2D nucleus (r^*) and larger activation energy for phase transition (ΔG^*). (c) Molar Gibbs energy difference, $G_{T_d} - G_{2H}$, as a function of temperature. G_{T_d} is always smaller than G_{2H} above 987 $^{\circ}\text{C}$. (d) Surface energy difference between T_d- and 2H-MoTe₂. T_d-MoTe₂ has a higher surface energy than 2H-MoTe₂ for all layer numbers. Ins

et: the gap of surface energy between 2H and T_d as a function of number of layers. For multi-layered T_d - MoTe_2 , the energy difference is almost the same; however, this is not the case for monolayer T_d - MoTe_2 .

However, the large transition temperature difference between the monolayer and bilayer, which deviates from the theoretical prediction that account only for surface and activation energies. Instead, I found that additional factors, such as charge carrier density and pressure, must be considered to explain the anomalously high phase transition temperature for monolayer MoTe_2 . First, during the thermal expansion of encapsulated MoTe_2 at high temperature, MoTe_2 is compressed along the c-axis because the hBN encapsulation limits the volume expansion of MoTe_2 . Second, the charge carriers of both electrons and holes are thermally excited in MoTe_2 . Our first-principles calculations reveal that the applied pressure reduces the energy of T_d , and the increased charge carrier density lowers the barrier energy for the phase transition (Figure 14). It is estimated that the monolayer has a smaller pressure than the thicker. Moreover, the monolayer has a smaller density of thermally excited electrons and holes at the fixed temperature than the thicker because of the larger band gap.⁽⁹⁷⁾ Therefore, the monolayer needs a much higher temperature for the 2H-to- T_d transition, probably due to the combinational effect of the smaller charge carrier density and reduced pressure in the vdW heterostructures.

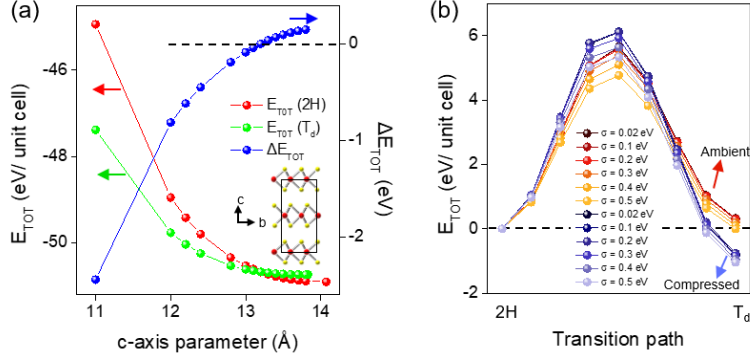


Figure 14. Effects of pressure and charge carrier density on the phase transition of MoTe₂. (a) First-principles calculations for the total energy per unit cell of 2H- and T_d-MoTe₂ as a function of the *c*-direction lattice parameter. The T_d phase is more stable than the 2H phase below *c*-direction lattice parameter of around 13 Å. (b) Energy landscape of phase transition under ambient and compressed (*c* = 12 Å) conditions. Charge carrier density was qualitatively described by the Fermi-smearing method (σ = Fermi-smearing width). Red- and blue-line circles show non-pressed and compressed conditions, respectively. Under ambient conditions, I observed that the barrier energy for the transition substantially decreases with increasing charge carrier density while the total energy per unit cell of T_d-MoTe₂ decreases slightly. In compressed conditions, albeit the barrier energy is higher than that of the ambient ones, the barrier energy decreases with increasing the charge carrier density.

Notably, I observe an *increase* in phase transition temperature for thinner

layers, a result that stands in stark opposition the trends in phase stability of conventional nanocrystals, which exhibit a *decrease* in T_{PT} with decreasing size (Figure 15).(98-106) These results indicate differences in the mechanisms of phase transition between the 2D materials and conventional nanocrystals. Nucleation of the newly formed phase in conventional nanocrystals generally occurs on a disordered surface, which would promote nucleation in smaller nanocrystals regardless of the surface energy difference.

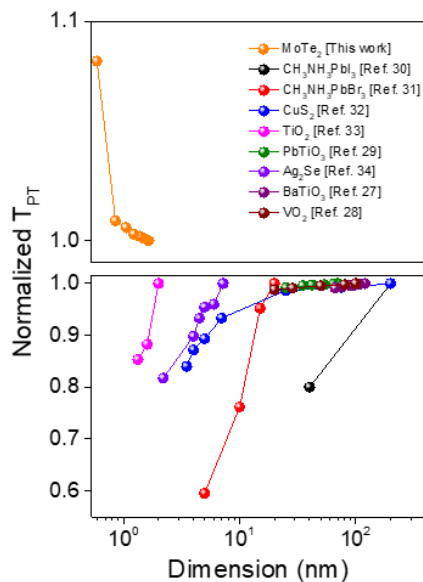


Figure 15. Size-dependent phase transition temperature of various nanoparticles and MoTe₂. To illustrate the size-dependent phase transition temperature variation, I normalized the phase transition temperature based on that in a large dimension scale. In general, the smaller nanoparticles show lower T_{PT} , which is contrary to our observation that T_{PT} increases with decreasing number of layers.

I measured the electrical properties of the transformed T_d phase. T_d - MoTe_2 of 7L is completely metallic with a low resistivity of $6.7 \times 10^{-3} \Omega \cdot \text{cm}$, which is similar to a previously measured value (Figures 16, a to c).⁽⁶⁶⁾ To fabricate 2H- MoTe_2 transistors with T_d contacts, I utilized the dimensionality-driven phase patterning technique. By annealing the as-exfoliated 2H- MoTe_2 consisting of 2L and 8L regions, I fabricated 8L- T_d contacts for the 2L-2H channel as shown in Figures 16, e to f. The device showed typical ambipolar transport behavior with linear I_{DS} - V_{DS} curves, indicating that ohmic contacts formed at the lateral junction of 2H and T_d . The field-effect mobility (μ_{eff}) of hole is $7.86 \text{ cm}^2/\text{Vs}$. The contact resistance of 2H- T_d junction calculated by Y-function method is $372 \Omega \cdot \mu\text{m}$ (see Supplementary Information for details of the calculation).⁽¹⁰⁷⁾ This value is comparable to the low contact resistances of the metallic phase contacts of 1T through lithiation and 1T' through electrical breakdown and CVD synthesis.^(80, 108, 109)

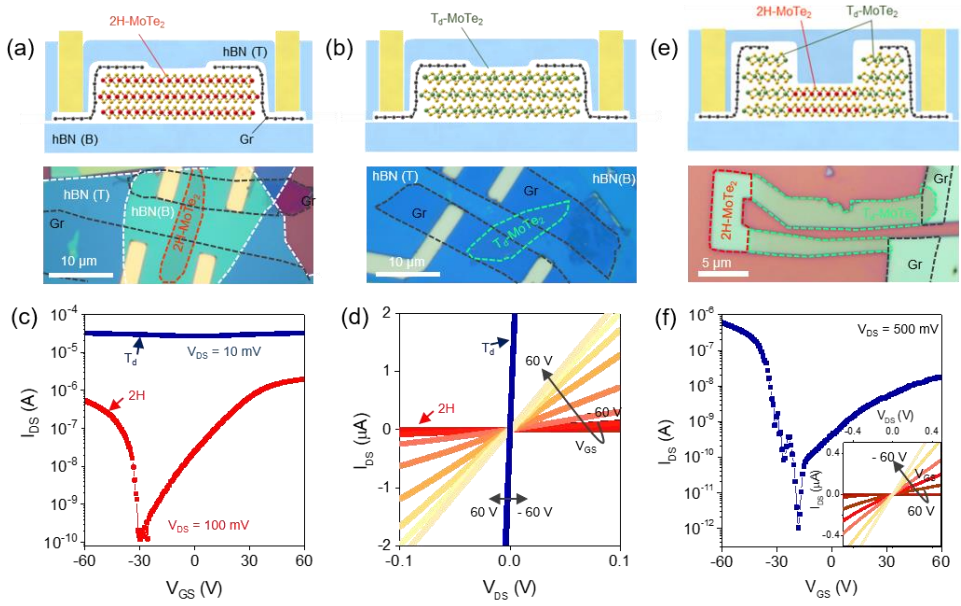


Figure 16. Phase-engineered 2H-MoTe₂/T_d-MoTe₂ heterophase devices. (a and b) Schematic illustrations and optical microscope images of hBN-encapsulated 2H-MoTe₂ and T_d-MoTe₂ devices with graphene contacts. (c) I_{DS} - V_{GS} characteristics for 2H- and T_d-MoTe₂ channel devices. The 2H-MoTe₂ device showed an ambipolar semiconducting characteristics, meanwhile T_d-MoTe₂ showed high I_{DS} without gate dependence, which indicates that T_d-MoTe₂ is metallic. (d) I_{DS} - V_{DS} characteristics for 2H- and T_d-MoTe₂ channel devices as a function of back-gate voltage V_{GS} ranging from -60 to 60 V. (e) Schematic representation and optical microscope image of a device with the T_d-2H monolithic heterophase junction in MoTe₂. (f) I_{DS} - V_{GS} characteristics for a monolithic heterophase junction device as a function of back-gate voltage V_{GS} ranging from -60 to 60 V. The device has semiconducting characteristics with a current I_{on}/I_{off} of 10^6 . The inset shows

a linear behavior in the I_{DS} – V_{DS} curves, indicating that typical ohmic contact formed at the junction of 2H and T_d .

3.1.3.3 Phase transition of the artificially-stacked MoTe₂

To investigate the effect of dimensionality, such as the thickness and stacking order of the vdW heterostructure, on the phase transition of MoTe₂, I fabricated a randomly stacked heterostructure of two MoTe₂ flakes with different thicknesses. Monolayer graphene was partially inserted to weaken the coupling between stacked MoTe₂ layers, as depicted in Figure 17a. Figure 17b shows the optical images and Raman intensity maps of the annealed graphene-inserted heterostructure of 2L- and 8L-MoTe₂ at 995 °C, which is higher than the T_{PT} of 8L ($T_{PT,8L}$) and lower than that of 2L ($T_{PT,2L}$). The heterostructure consists of four areas: hBN/8L-MoTe₂/Gr/2L-MoTe₂/hBN, hBN/8L-MoTe₂/2L-MoTe₂/hBN, hBN/8L-MoTe₂/hBN, and hBN/2L-MoTe₂/hBN (denoted as B8MG2MB, B8M2MB, B8MB, and B2MB, respectively). Raman intensity maps for the E_{2g} mode of 2H-MoTe₂ and the A_1 mode of T_d -MoTe₂ reveals that the stacked and 8L areas transformed into the T_d phase, except for the 2L region. Note that the misaligned stacked region of 2L and 8L totally transformed into T_d even at the T_A lower than $T_{PT,2L}$. Furthermore, the B8MG2MB region, where the graphene is inserted between 2L and 8L, showed both Raman peaks of 2H and T_d , indicating the

coexistence of 2H and T_d .

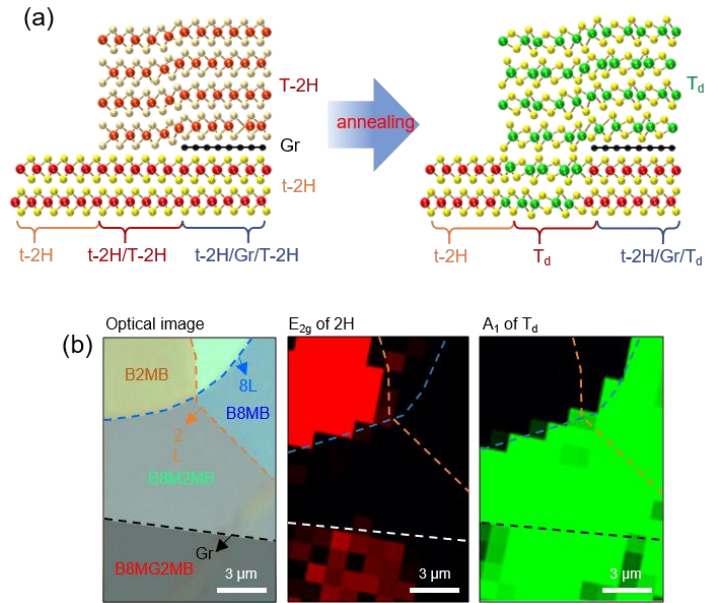


Figure 17. Phase transition of the stacked MoTe_2 layers with an inserted monolayer graphene. (a) Phase transition process of the randomly stacked MoTe_2 flakes with an inserted monolayer graphene. The thin and thick 2H- MoTe_2 with different phase transition temperatures are denoted as t-2H and T-2H, respectively. When the stack was annealed at $T_{\text{PT,thick}} < T_A < T_{\text{PT,thin}}$, the stacked and thick regions (t-2H/T-2H and T-2H) were changed to the T_d phase, except for the thin region and graphene-inserted region. (b) Optical image and Raman intensity mapping images of annealed monolayer graphene inserted thin MoTe_2 / thick MoTe_2 heterostructure. B8MG2MB, B8M2MB, B8MB, and B2MB indicate the areas of $\text{hBN}/\text{MoTe}_2(8\text{L})/\text{Gr}/\text{MoTe}_2(2\text{L})/\text{hBN}$, $\text{hBN}/\text{MoTe}_2(8\text{L})/\text{MoTe}_2(2\text{L})/\text{hBN}$, $\text{hBN}/\text{MoTe}_2(8\text{L})/\text{hBN}$, and $\text{hBN}/\text{MoTe}_2(2\text{L})/\text{hBN}$. Under annealing at the temperature where B2MB does

not change its phase, phase transition occurred at B8MB, B8M2MB, and B8MG2MB.

To verify the effect of the inserted graphene on the phase transition, I measured the SAED patterns of the B8M2MB and B8MG2MB regions. In the B8M2MB region, only signals of a single T_d phase were observed without any remaining 2H phase, as indicated by the green rectangle in Figure 18a. Several diffraction spots are originated from hBN and multiple scattering at the heterointerface.⁽¹¹⁰⁾ This result reveals that, as depicted in Figure 18c, the 2L region changed to the T_d phase with the same crystalline alignment to the 8L region, despite a twist angle of 8° in the as-stacked sample. The stacked crystals appeared to rotate reduce the interfacial energy induced by misalignment with the help of pressure and thermal energy during the annealing process.^(111, 112) Meanwhile, the graphene-inserted heterostructure of B8MG2MB exhibited SAED patterns of both 2H and T_d phases with misalignment, as shown in Figure 18b. Only 8L-MoTe₂ transformed into T_d , and there was no phase transition or crystalline rotation of the 2L-MoTe₂ owing to weakened coupling between 2L- and 8L-MoTe₂ due to the inserted graphene, as shown in Figure 18d. Therefore, this result indicates that the phase transition of MoTe₂ in the vdW heterostructure can be controlled by dimensionality of thickness and stacking order, which enables phase patterning of MoTe₂ along the lateral and vertical directions.

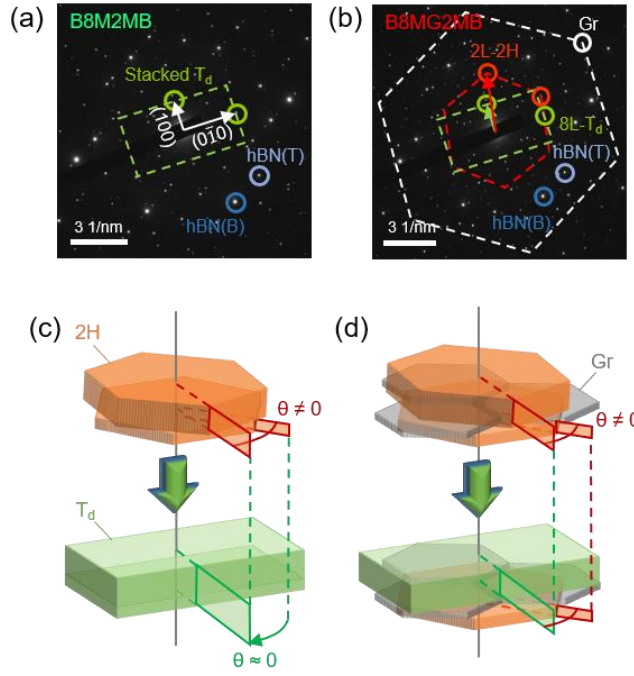


Figure 18. (a and b) Selective area electron diffraction patterns in B8M2MB, and B8MG2MB. After annealing, the misaligned stack of 2L and 8L of 2H-MoTe₂ with a twist angle transforms into aligned T_d-MoTe₂ with zero twist angle. (c and d) Schematic illustrations of the crystal orientation rotation of B8M2MB and B8MG2MB. Inserted graphene hindered coupled phase transition phenomena, which could result from increased interface energies for MoTe₂ (2L)/Gr and MoTe₂ (8L)/Gr.

2.1.4 Conclusions

I have demonstrated an anomalous dimensionality-driven phase transition of MoTe₂ by using encapsulated annealing within hBN. I

transformed the single-crystalline 2H-MoTe₂ into high-quality polycrystalline T_d-MoTe₂, which only has a 60° difference in all the grains. Phase transition of MoTe₂ has thickness-dependence; T_{PT} increases with decreasing number of layers due to highly ordered surface structure of MoTe₂ with no dangling bonds and higher surface energy of T_d-MoTe₂ than 2H-MoTe₂. The thickness-dependent phase transition occurs even in a stack of two MoTe₂ flakes with different crystallographic orientations. The coupled phase transition can be controlled by inserting monolayer graphene between stacked MoTe₂ flakes. The dimensionality-driven phase transition of MoTe₂ in van der Waals heterostructure opens new possibilities for developing three-dimensional phase patterning and monolithic 2D electronic devices consisting of different phases of the same 2D materials.

2.2. Laser-induced phase transition of MoTe₂

2.2.1 Introduction

Phase transition of ultrathin transition metal dichalcogenides (TMDs) have attracted extensive attention owing to a low energy barrier for phase transition and various phases with different physical properties. Among them, MoTe₂ have shown that 2H phase can transform into 1T' phase by various stimuli.⁽¹¹³⁾ Therefore, different methods, such as annealing, electrostatic doping, tensile strain, plasma treatment, and electric field, have been used to trigger phase transition of 2H phase into a different phase, such as 1T', T_d, and 2H_d.^(71-74, 76, 77, 114-119) Among these phase transition techniques, laser-induced phase transition is very useful for practical applications because MoTe₂ can be patterned into metallic 1T' and semiconducting 2H regions through a lateral junction². On the other hand, it was also reported that the laser -induced metallic phase is just Te clusters due to vigorous evaporation, not 1T' phase.^(71, 120-122) These results show that defect formation by evaporation of atoms and control of temperature are main factors to determine the type of phase after phase transition.^(120, 123, 124)

Here, I show laser-induced phase transition and patterning of hBN-encapsulated 2H-MoTe₂ to laterally stitched 2H-1T' heterointerface. I used hBN-encapsulation to prevent evaporation of MoTe₂ during laser annealing. In addition, temperature of MoTe₂ obtained by the laser irradiation was

different owing to distinctive heat dissipation characteristics of adjacent materials, such as air, hBN, and SiO₂. As a result, I observed phase transition of 2H-MoTe₂ into various phases, such as 1T'-MoTe₂, Mo₃Te₄, and Te. However, when the 2H-MoTe₂ was perfectly encapsulated by hBN, the single crystal 2H-MoTe₂ transformed into polycrystalline 1T' phase with thickness-dependent phase transition temperatures. By using local heating by the laser, I fabricated the MoTe₂ device with a channel of 2H and contact of laterally stitched 2H-1T' heterointerface, which allows for high mobility and low contact resistance.

2.2.2 Experimental procedure

Stacking process and laser irradiation

Stacking process is same as described in chapter 3.1. To heating the hBN-MoTe₂ vdWs heterostructures, I used 2.33 eV continuous laser with a power of 20.4 mW, focused by 100× objective lens (N.A. = 0.9). The laser irradiation area was patterned with 200 nm point-to-point distance and 0.1 s exposure time. All of laser irradiation was done at ambient condition.

Raman spectroscopy

Raman spectra measurement condition is same as described in chapter 3.1.

Transmission electron microscopy

S/TEM measurement condition is same as described in chapter 3.1.

Device fabrication and electrical measurement

Device fabrication process and electrical measurement condition is same as described in chapter 3.1.

Temperature distribution calculations

Temperature distribution calculations are done by finite element methods, using commercial software package COMSOL Multiphysics. Thermal conductivity of hBN (125); MoTe₂ (126); SiO₂ (127); Si (128), and optical property of SiO₂ (129); MoTe₂ (130); Si (131); air (132) were used for calculations. I set the thickness of hBN and MoTe₂ for 5 nm and 4 nm, and highly-doped Si wafer covered by 285 nm SiO₂ is used for substrate. I set the laser irradiation environments like experimental conditions: 2.33 eV laser with 20.4 mW was irradiated to 2D layer, with 1 um diameter spot with gaussian intensity profile. Imaginary refractive index of materials is set to 0 except MoTe₂ and Si. All other light dissipation mechanism except reflection/refraction by refractive index difference and absorption by imaginary refractive index, Rayleigh scattering, absorption by transparent media (SiO₂ and air), etc., were neglected. Air convection was also neglected.

2.2.3 Results and discussions

2.2.3.1 Phase and chemical composition control of MoTe₂ by laser irradiation and heat dissipation in van der Waals heterostructures

Figure 19a shows a phase diagram of the Mo-Te system at atmosphere pressure.⁽¹³³⁾ MoTe₂ shows phase transition from 2H to 1T' around 880 °C. However, the 1T'-MoTe₂ is separated into two phases of Mo₃Te₄ and gaseous Te above 1180 °C. At 1300 °C, the MoTe₂ starts to be decomposed into Mo metal and gaseous Te. This indicates that the MoTe₂ can have various phases and compositions, such as 2H-, 1T'-MoTe₂, Mo₃Te₄, and Te, during annealing process, depending on the temperature and evaporation of Te. Figure 19b shows crystal structures of different phases that I can achieve after annealing process.

To investigate the effect of encapsulation and laser annealing temperature on the phase transition of MoTe₂, I prepared different stacks by transferring exfoliated flakes of MoTe₂ and hBN on a SiO₂ substrate via the pick-up technique as shown in Figure 19c: MS (MoTe₂ / SiO₂), MB (MoTe₂ / hBN), BMS (hBN / MoTe₂ / SiO₂), and BMB (hBN-MoTe₂-hBN).⁽¹³⁴⁾ MS and MB are exposed to air, meanwhile BMS and BMB are passivated by the hBN to prevent evaporation of the MoTe₂. I used the 5 nm-thick hBN because it acts as efficient heat dissipator and passivation layer owing to high in-plane

thermal conductivity, polar phonons (hyperbolic phonon polaritons), high thermal stability, and impermeability.(115, 135, 136) I used a continuous wave laser of 2.33 eV as a heating source (See detailed conditions for laser irradiation in the Experimental procedure). The light can be selectively absorbed only by the MoTe₂ with smaller bandgap of 1 eV than the energy of photons.(137, 138) The thermal energy transformed from absorbed optical energy through lattice vibration induces thermalization of optically-excited hot electrons. In Figure 19c, I also estimated the temperature distribution of each stack under laser irradiation by using finite element method. The hBN of 5 nm and 2H-MoTe₂ of 4 nm were used in the calculations. I set the laser irradiation environments like experimental conditions: 2.33 eV laser with 20.4 mW was irradiated with 1 μm diameter spot with gaussian intensity profile. The air-exposed structures of MS and MB showed the maximum temperatures, much higher than melting temperature of MoTe₂, at top surface of MoTe₂ due to low heat transfer between MoTe₂ and air. Meanwhile, hBN-passivated structures of BMS and BMB showed the maximum temperatures in the middle of MoTe₂ due to the efficient heat dissipation to the hBN. Note that the maximum temperature of BMB is lower than that of BMS owing to larger heat dissipation by the hBN. Figure 19d shows the estimated maximum temperatures of the MoTe₂ in the BMB (green) and MB (pink) structures as a function of laser power. The maximum temperature of the BMB structure is higher than that of the MB structure over all laser power range. Therefore, I

need a higher laser power of 18 mW to achieve the 2H-to-1T' phase transition temperature (T_{PT}) of 880 °C in the BMB, compared to 11 mW for the MB.

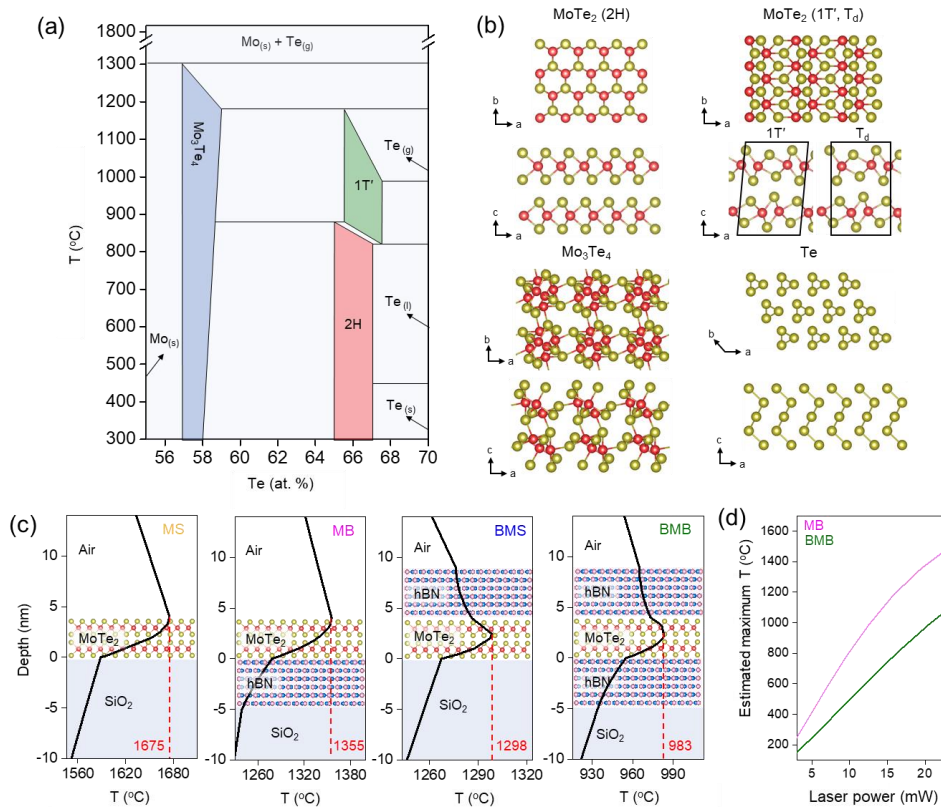


Figure 19. Laser-induced thermalization of MoTe₂ and heat dissipation in van der Waals heterostructures. (a) Phase diagram of Mo-Te system at atmospheric pressure. (b) Schematic images of various thermodynamically stable phases in the Mo-Te system. (c) Spatial temperature distribution under laser irradiation calculated by finite element method. Since the thermal conductivity of hBN, SiO₂, and air are different, the temperature distribution of MoTe₂ varies depending on the type of material adjacent to MoTe₂.

hBN/2H-MoTe₂/hBN, hBN/2H-MoTe₂/SiO₂, 2H-MoTe₂/hBN, and 2H-MoTe₂/SiO₂ are denoted as BMB, BMS, MB, and MS, respectively. (d) The calculated maximum temperature (T_M) in MoTe₂ as a function of laser power. In BMB structure, the T_M reaches the phase transition critical temperature at 18 mW laser power. Meanwhile, in MB structure, only 11 mW laser power is needed to attain phase transition.

Figure 20a shows the Raman spectra of 2H-MoTe₂ (4L) in the different stacks of BMB, BMS, MB, and MS after laser irradiation (2.33 eV laser with 20.4 mW power). As-exfoliated 2H-MoTe₂ typically shows three Raman peaks of E_{2g}, A_{1g}, and B_{2g}. After laser irradiation, BMB structure showed the several Raman peaks, which correspond to A_g and B_g modes of the 1T' phase with no remaining Raman peaks of 2H phase. Additionally, measured linearly-polarized Raman spectrum of the BMB structure at a low-frequency range shows that 4L 2H-MoTe₂ transformed into the 1T' phase, which is in agreement with our previous report.^(93, 114, 139) In contrast, the other stacks of BMS, MS, and MB clearly showed the Raman peaks of Te. Note that MS and MB showed remaining peaks of the 2H phase. Figures 20, b-e show optical microscopic images of the stacks after the laser irradiation. The MS and MB stacks showed a clear contrast change due to evaporation and etching during laser irradiation. Even though the BMS was passivated by hBN, laser-irradiated region showed severe damage. Meanwhile, the BMB showed no

recognizable change in contrast as shown in Figure 20e. Raman peak intensity map was obtained from E_{2g} of 2H and A_g of 1T' as shown in the inset of Figure 1e. The laser-irradiated region is uniformly transformed into the 1T' phase with lateral junction with the 2H phase regions.

Emergence of different phases in Raman spectra of Figure 20a can be explained in terms of the phase diagram and calculated temperature distributions. The maximum temperature of laser-irradiated BMB structure is close to the 2H-to-1T' phase transition temperature in the phase diagram. However, the maximum temperatures of the other stacks are higher than the decomposition temperature of $MoTe_2$ so that other phases of Mo_3Te_4 and Te can be produced by decomposition and recrystallization. The 2H phase in the bottom layers of $MoTe_2$ in the MB and MS stacks is maintained due to cooling effect by the SiO_2 , meanwhile the top layers of the $MoTe_2$ are evaporated first due to low thermal conductivity of air, leading to the MoO_x and Te crystals. It is worth noting that the Raman peak intensity of 2H phase in the MS is higher than that in the MB because of higher temperature of the MS.

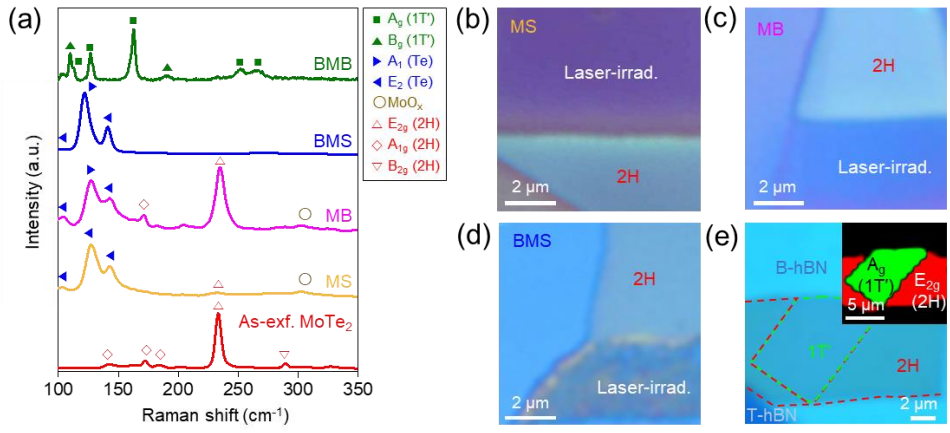


Figure 20. Raman spectra and optical images of MS, MB, BMS, and BMB structures after laser irradiation. (a) Raman spectra of MoTe₂ for 2H-MoTe₂, MS, MB, BMS, and BMB structures. (b-c) Optical images of MS, MB, and BMS structures after laser irradiation. (e) Optical image BMS structures after laser irradiation. Inset: Raman intensity map from A_g mode of 1T' phase and E_{2g} mode of 2H phase.

To investigate the crystal structure of the laser-irradiated MoTe₂, I used transmission electron microscopy (TEM) as shown in Figure 21. Because the thick hBN is not transparent to electron beam, monolayer graphene was used as an encapsulation layer for TEM observation. The MoTe₂ was encapsulated by monolayer graphene and thick hBN flakes, followed by laser irradiation to induce the phase transition. Then, the hBN was etched by using graphene etching stop (GES) technique.⁽¹¹⁵⁾ (see Methods for details in the TEM sample preparation). The atomic structure of the graphene-encapsulated

MoTe₂ can be clearly observed by TEM because of the low contrast of the carbon atoms.⁽⁹⁵⁾ TEM image of the laser-irradiated region in the MS shows randomly distributed nanograins of the Te with an average size of ~20 nm, which is verified by diffraction pattern (DP) in inset of Figure 21a and the Raman spectrum of the MS in Figure 20a. In the DP of Figure 21a, I can observe the hexagonal diffraction spots of the single 2H (red line) and multiple spots of the Te nanograins (yellow line). It is because the top layers of MoTe₂ was recrystallized into the Te nanograins and bottom layers of 2H phase are maintained, which is in line with previous results.^(71, 120-122) Note that a number of spots are originated from randomly distributed Te nanograins. The laser-irradiated BMS has voids and isolated regions of Mo₃Te₄ and Te as shown in Figure 21b. Non-uniform distribution of elements was verified by the EDS elemental mapping (Inset of Figure 21b). I used high-angle annular dark-field scanning transmission electron microscopy (HAADF-STEM) to confirm the crystal structures of the isolated regions (blue and green dashed regions in Figure 21b). Figure 21c clearly shows the atomic structures of the crystalline Te (blue dashed region) and Mo₃Te₄ (green dashed region), which are well matched with the atomic models as shown in the insets of Figure 21c.⁽¹⁴⁰⁾

In contrast, the false-color dark field (DF)-TEM image of Figure 3d shows that the laser-irradiated BMB has well-stitched irregular 1T' grains of a few hundred nanometers. The DPs of 2H and 1T' regions in Figure 3e show

that 2H and 1T' are crystallographically aligned and polycrystalline 1T' grains have 60° difference in the crystallographic directions.(72, 75) All 1T' grains are well-stitched along two preferred grain boundaries of 120° twofold rotation and 60° glide-reflection as shown in Figure 21f, which is similar to the previous results.(96, 115) More surprisingly, I clearly observed an atomically sharp heterointerface between 2H and 1T' phases. It indicates that atomically sharp heterointerface can be fabricated without massive atomic loss and destruction in the millisecond-scale laser heating of hBN-encapsulated MoTe₂.

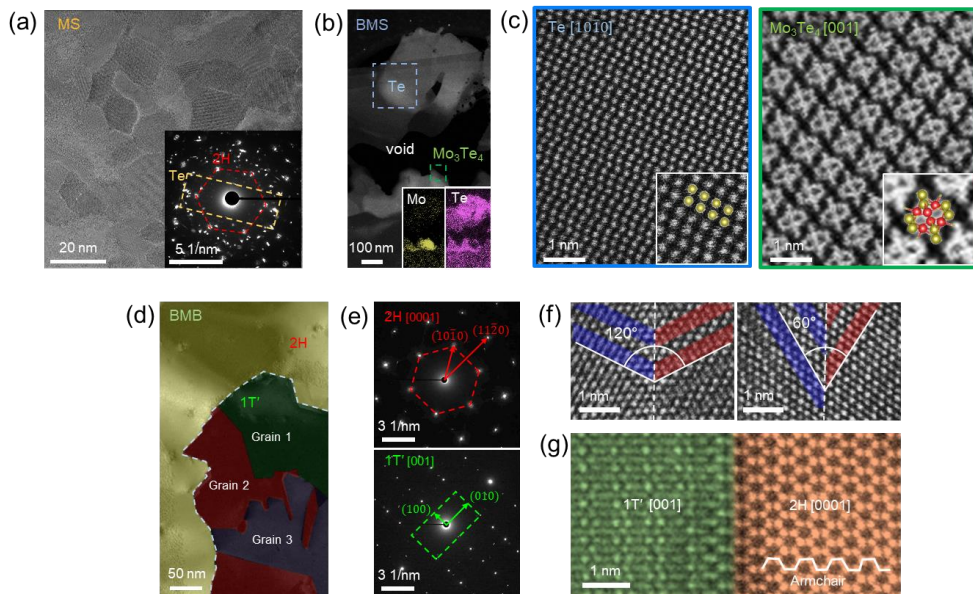


Figure 21. Plan-view S/TEM images of laser-irradiated stacked structures. (a) TEM image of MS structure after laser irradiation. Inset: diffraction pattern of MS structure. 2H-MoTe₂ and randomly-oriented Te are observed. (b) BF-TEM image and EDS mapping images of Mo and Te of BMS structure.

Reorganization of thermally-degraded MoTe₂ generates Te-rich and Mo-rich areas. (c) HAADF-STEM images of Te-rich and Mo-rich area in Figure 21b. Te-rich and Mo-rich areas consist of crystalline Te and Mo₃Te₄. (d) False-color DF-TEM images of laser-irradiated BMB structure. The Laser-irradiated area is transformed from 2H into 1T' phase. 1T'-MoTe₂ is polycrystalline, and grain 1, 2, and 3 have only a 60° crystallographic direction difference because the armchair-direction-aligned atomic slide in pristine 2H-MoTe₂ is energetically favorable. (e) Diffraction patterns of 2H- and 1T'-MoTe₂. The red and green dashed lines indicate the crystal symmetries of 2H and 1T' phases, respectively. The other spots are generated from the graphene and multiple diffraction of electron beam at the interfaces. (f) HAADF-STEM image of the 120° twofold rotation GB and 60° glide-reflection GB in polycrystalline 1T'-MoTe₂. g, HAADF-STEM image of an atomically sharp interface between 2H and 1T' phase.

2.2.3.2 Laser power and layer number dependent phase changes under laser irradiation

When the 4L MoTe₂ flakes in the BMB and MB structures were irradiated with different laser powers (2.3, 4.2, 9.9, and 20.4 mW), the 2H phase was maintained at low laser power. Meanwhile, in BMB structure, the 1T' phase emerged at 20.4 mW owing to higher maximum temperature than

T_{PT} as shown in Figure 19d and 22a. In case of the MB structure, only Raman peaks of Te were observed even at much lower laser power of 9.9 mW due to the evaporation of MoTe_2 as shown in Figure 22b. Even at higher laser power of 20.4 mW, the MB structure showed no Raman peaks of 1T' phase except for Te and 2H phases. The reduced Raman peaks of 2H at 20.4 mW indicates that MoTe_2 was etched by the laser.(71) This result shows that the hBN encapsulation prevents the evaporation of MoTe_2 during laser irradiation, which allows for the 2H-to-1T' phase transition without structural degradation. To verify thickness dependence of the phase transition in MoTe_2 , hBN-encapsulated 2H- MoTe_2 flakes with different thicknesses of 1-5L were annealed by the laser of the same power (20.4 mW) as shown in Figure 22c. After laser irradiation, the MoTe_2 thicker than 4L showed the phase transition into the 1T' phase, meanwhile thin MoTe_2 flakes showed no change, which is in agreement with our previous result that the thinner MoTe_2 has the higher T_{PT} .(115)

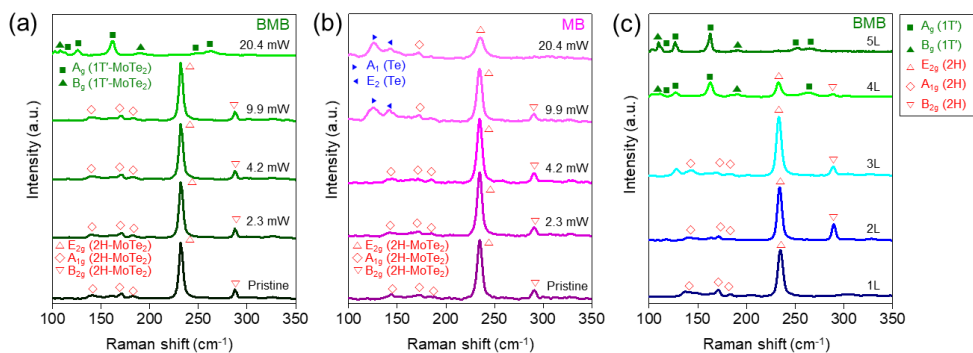


Figure 22. Laser power and layer number dependent phase changes in BMB,

MB structures. (a-b) Raman spectra of BMB, MB structure after irradiation of different power of laser. In BMB structure, only laser power of 20.4 mW induced phase transition from 2H to 1T' phase. However, in MB structure, Te defects were generated even at laser power of 9.9 mW. (c) Raman spectra of MoTe₂ as a function of layer numbers in BMB structure. Phase transition is induced in more than 4 layers.

2.2.3.3 Laser-induced 2H–1T' monolithic heterophase devices

To measure the electrical properties of the BMB structure, I fabricated the hBN-encapsulated MoTe₂ device with graphene electrodes (Figure 23a). The optical image and Raman intensity maps of Figure 23b show that 2H-MoTe₂ region between graphene electrodes locally transformed into the 1T' phase after the laser irradiation. Figures 23, c and d represent the transfer curves ($I_{DS}-V_{GS}$) and output curves ($I_{DS}-V_{DS}$) of the BMB before and after the laser irradiation. As shown in the transfer curves of Figure 23c, the semiconducting 2H-MoTe₂ with ambipolar characteristics totally changed to the metallic 1T' phase with no gating effect. The output curves of Figure 23d also shows the resistivity of 1T'-MoTe₂ is as low as $7.52 \times 10^{-2} \text{ k}\Omega \cdot \mu\text{m}$, comparable to that of polycrystalline T_d-MoTe₂.(115)

Because the low resistance 1T' phase can be patterned with well-stitched junction to the 2H region by the laser irradiation, I fabricated the top-gated

2H-MoTe₂ device with lateral junction of the metallic 1T' phase by patterning the contact regions as shown in Figures 23, e and f. The transfer curves of Figure 23g clearly shows ambipolar transport characteristics with a field-effect mobility of 16.11 cm²/Vs for electron and 3.9 cm²/Vs for hole, high on/off ratio of 10⁷, and low subthreshold swing (SS) of 66 mV/dec. The superior device performance is attributed to the suppressed charged impurity scattering by hBN-encapsulation and low contact resistance.⁽¹⁴¹⁾ As shown in Figure 23h, the linear output curves indicate that the 2H-1T' heterointerface with well-stitched grain boundary has a low contact barrier. The contact resistance of the 2H-1T' junction measured by the Y-function method was 1.13 kΩ·μm.^(107, 142) This value is comparable to the reported values of 2H MoTe₂ transistors with a similar in-plane heterophase structure.^(81, 109, 116, 143) I note that our 2H-1T' junction device firstly shows ambipolar transport behavior in heterophase junction MoTe₂ devices in contrast to other previous results.

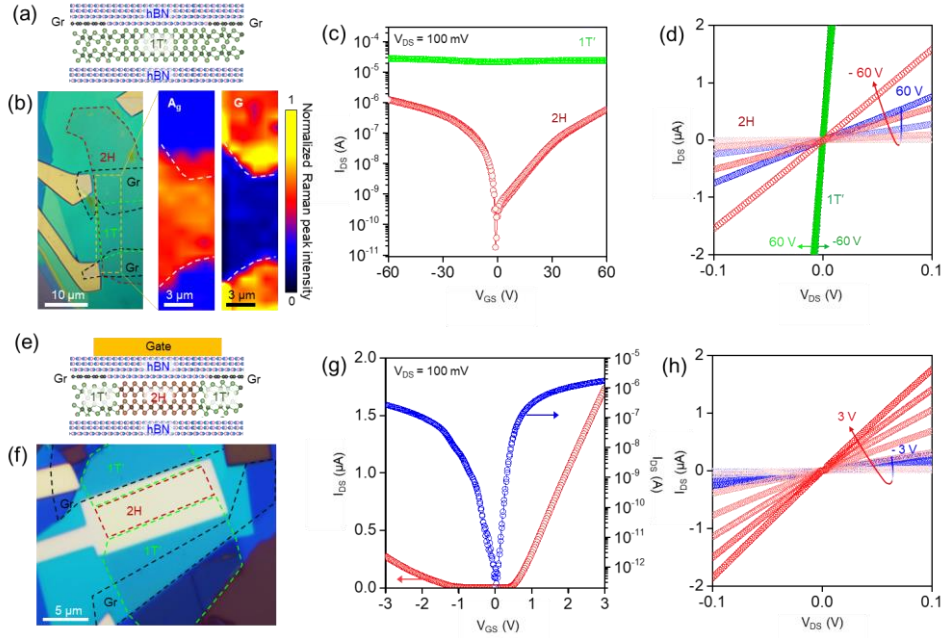


Figure 23. Device properties of laser-irradiated 2H-1T' monolithic heterophase devices. (a) Schematic images of 1T' channel device with graphene contact. (b) Optical image and Raman peak intensity map images of laser-induced 1T'-MoTe₂ device with graphene contact. Raman peak intensity map images of A_g mode of 1T'-MoTe₂ and G mode of graphene identify the channel and contact area. (c) I_{DS} - V_{GS} curves for 2H- and 1T'-MoTe₂ channel devices. Before laser irradiation, the 2H-MoTe₂ channel device showed ambipolar characteristics. Meanwhile, after irradiation, 1T'-MoTe₂ channel showed metallic properties. (d) I_{DS} - V_{DS} characteristics for 2H- and 1T'-MoTe₂ channel devices as a function of back-gate voltage V_{GS} ranging from -60 V to 60 V. (e) Schematic image of 2H-1T' monolithic heterophase device. (f) Optical image and schematic illustration of the 2H-1T' monolithic heterophase device. (g) I_{DS} - V_{GS} characteristics for the 2H-1T'

monolithic heterophase device as a function of back-gate voltage V_{GS} ranging from - 3 V to 3 V. The device has semiconducting characteristics with a current I_{on}/I_{off} of 10^7 . (h) $I_{DS}-V_{DS}$ characteristics for the 2H-1T' monolithic heterophase device. Linear behavior of $I_{DS}-V_{DS}$ curves indicates typical Ohmic contact is formed at the junction of 2H and 1T'.

2.2.4 Conclusions

In conclusion, I show the stable phase transition of $MoTe_2$ by laser irradiation to achieve laterally stitched 2H-1T' heterointerface. hBN encapsulation prevents the evaporation of surface layer during laser irradiation and dissipates accumulated heat, which enables stable phase transition of $MoTe_2$ from single crystal 2H phase to polycrystal 1T' phase in patterned area. In other opened or single-side passivated structure, chemical composition of $MoTe_2$ was changed after laser irradiation from the evaporation or etching process. I also observed the layer number dependent phase transition behavior in hBN-encapsulated $MoTe_2$. The laser-induced 1T'- $MoTe_2$ shows metallic properties with low resistivity, and 2H-1T' monolithic heterophase device shows ambipolar transport and low contact resistance of $1.13 \text{ k}\Omega \cdot \mu\text{m}$. The stable phase transition of hBN-encapsulated $MoTe_2$ under laser irradiation opens new possibilities of the monolithic phase patterning of 2D materials

2.3. Anisotropic layer-by-layer phase transition of MoTe₂

2.3.1 Introduction

Understanding the phase transition kinetics and mechanism of 2D materials is the key to precisely tailor their properties at the nanoscale. Few-layer MoTe₂ is particularly interesting because it shows multiple phases at room temperature with distinct properties, making it promising candidate for phase-change memories, high-performance transistors, and broadband photodetectors.

As shown in chapter 2.1 and 2.2, 2H-to-1T' phase transition was demonstrated with high temperature annealing of few-layer, encapsulated MoTe₂. The integration of a semiconductor with topological phases based on the same compound may open up new possibilities towards low dissipation 2D electronics and spintronics. However, the 2H-to-1T' phase transition mechanism remains largely unexplored.

In situ TEM is a powerful technique that can detect structural changes of materials with various stimuli.^(75, 144) However, electron beam irradiation and vacuum annealing have been reported to cause major degradation of MoTe₂ from the loss of Te atoms, making it particularly challenging to unveil the phase transition process without altering the chemical composition.^(95, 145, 146) The graphene encapsulation can prevent sublimation of MoTe₂ during heating and contributes minimal background signal to the imaging

process, which is critical for atomic resolution imaging.

Here I use graphene encapsulation to create an enclosed reaction cell for in situ TEM studies of the phase transition mechanism of 2H- and 1T'-MoTe₂ from micro- to atomic scales. I apply in situ pulsed heating to monitor the reverse phase transition kinetics of 1T'-to-2H with a combination of aberration-corrected STEM and Dark-field TEM. I find that the 1T'-to-2H phase transition initiates at the 2H/1T' interface at around 225 °C, much lower than the 900-1000 °C reported for 2H-to-1T' transition previously observed with annealing. I show that the 1T'-to-2H phase transition is highly anisotropic at low temperatures. Between 200-400 degrees °C, I observe that the 2H phase fronts primarily propagate along the b-axis of the 1T' grains, progressing in-plane and layer-by-layer motion with a temperature-dependent, diffusive character.

2.3.2 Experimental procedure

Sample preparation for in-situ TEM study

Stacking process and local phase patterning process are same with previous fabrication method in chapter 3.1 and 3.2. Exfoliated flakes were stacked by pick-up method, and then 1T' phase area was locally patterned by laser-irradiation.

Ex situ 1T'-to-2H phase transition with annealing

To re-transition phase from 1T' to 2H, I annealed phase-patterned sample in furnace. I annealed the laser-irradiated stacked MoTe₂ in a vacuum of 10⁻⁴ Torr by using furnace. The furnace temperature was increased up to the 800 °C for 3 h and maintained for 3 h. Then, the furnace was naturally cooled to room temperature.

Sample preparation for in situ imaging of phase transition

First, to image the MoTe₂ in atomic resolution, I etched hBN layers by XeF₂ gas exposure.⁽¹⁴⁷⁾ The laser-irradiated stacked MoTe₂ was picked up using PC-coated PDMS. The bottom hBN layer was etched away by XeF₂ exposure, and the etching process was self-stopped at graphene layer.⁽⁹¹⁾ And then, the stacked structure was transferred onto a SiO₂/Si substrate at 180 °C. The PC film was removed in chloroform for 1 hour. I used oxygen plasma to remove the remaining residue on top hBN layer. And the exposed top hBN layer was also etched away by the same XeF₂ exposure process. The fluorinated-graphene-encapsulated MoTe₂ was transferred onto a in-situ heating TEM grid (Protochips, E-FHDC-VO-10) using the PMMA transfer technique. The PMMA film was removed by acetone.

Raman spectroscopy measurement

Raman spectra were measured by same method in chapter 3.1 and 3.2.

In-situ heating and S/TEM measurement

In-situ heating experiments are done in a Thermo Fisher Scientific Themis-Z aberration-corrected S/TEM operated at 80 kV. For atomic-resolution ADF-STEM imaging, the point resolution is about 1 Å with 25 mrad convergence semi angle, 35 pA probe current, 63 to 200 mrad collection semi angles, 20 pm pixel size and a total dwell time of 20 μs/pixel using 10-frame averages. For BFTEM, SAED, and DFTEM, the data are acquired with a Ceta 16M camera at parallel illumination using the three-condenser TEM mode. The electron dose rate is around 10^3 e⁻/nm²/s and the exposure times for SAED and DFTEM are 2 to 5 s.

2.3.3 Results and discussions

2.3.3.1 Phase transition and recovery of MoTe₂ (2H→1T'→2H phase) via laser irradiation and annealing process

Figure 24 shows the schematic of reversible phase transition process of MoTe₂. To create an encapsulated cell, I fabricate hBN/graphene/MoTe₂/graphene/hBN heterostructures by the PDMS-assisted pick-up technique. The hBN/graphene encapsulation acts as physical and chemical barrier for MoTe₂, which minimizes the sublimation of Te or

interaction with the atmosphere during further processing. I then laser-irradiate the encapsulated 2H-MoTe₂ to locally initiate the phase transition of MoTe₂ from 2H to 1T' phase. The phases of pristine and laser-irradiated MoTe₂ are identified by both HAADF-STEM images (Figure 24, c and d) and Raman spectroscopy (Figure 24e).

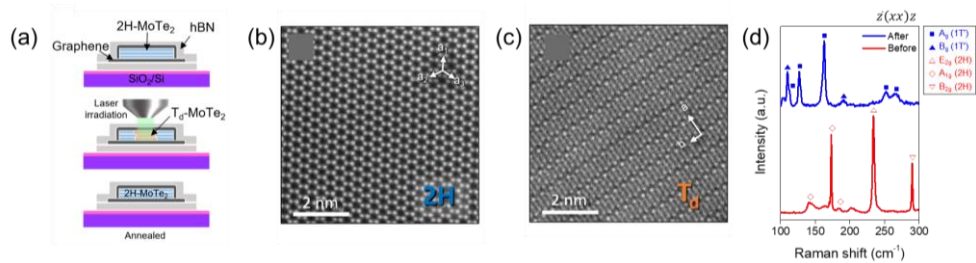


Figure 24. Characterization of different phases of MoTe₂. (a) Schematic of the reversible phase transition of MoTe₂. Local laser-irradiation induces 2H-to-1T' phase transition of MoTe₂, while the 1T'-MoTe₂ can be reverted back to 2H phase with an annealing process. (b-c) HAADF-STEM images for 2H and 1T' phase, respectively. (d) Raman spectra of 1T'- and 2H-MoTe₂.

To further investigate the 1T'-to-2H phase transition, I transfer the laser-irradiated, MoTe₂ specimens on a MEMS chip for in situ heating experiments. The 1T' phase was prepared with the same laser irradiation technique as described above, but the hBN layers are removed by XeF₂ dry etching for better imaging condition. Figure 25a is a bright-field TEM image with very little contrast between 2H and 1T' phases, indicating the uniform thickness across the 2H/1T' interface. I perform SAED (Figures 25, b and c) to

characterize the crystal structures of 2H and 1T' grains. The diffraction patterns of 2H and 1T' grains show their characteristic hexagonal and rectangular lattice, respectively. Next, I use dark-field TEM to map the location and orientation of phases in MoTe₂. Dark-field TEM has been widely used in determining crystal orientations of 2D crystals and operates by selecting specific Bragg spots in the diffraction pattern with an objective aperture.^(148, 149) Figures 25, d and g show dark-field TEM images of 2H and 1T' phases, formed respectively by selecting the (-1100) 2H and (-210) 1T' Bragg reflections. I observe three distinct orientations of 1T' grains, rotated 120 degrees from each other and corresponding to 3-fold symmetry of the 2H phase. Figure 25f shows a false-colored dark-field TEM overlay of images mapping the four distinct crystal phases and orientations present after laser-irradiation: the 2H-phase (in red) and the three 1T' orientations (green, yellow, and blue).

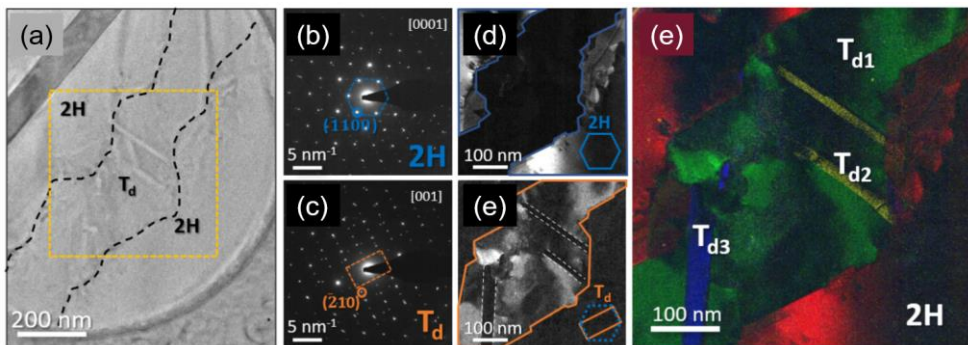


Figure 25. Phase and grain orientation mapping of laser-irradiated MoTe₂ with TEM. (a) Bright-field TEM image of the suspended MoTe₂ containing both 2H and 1T' grains. The 1T' phase region was delineated by the laser

trajectory and outlined by the black dashed lines. (b-c) Selected-area electron diffraction patterns, (d-e) dark-field TEM images of 2H and 1T' phase, respectively. The diffraction patterns (b-c) are acquired with zone axis perpendicular with the basal planes. The Dark-field TEM images (d-e) are formed by selecting the (-1000) 2H and (-210) 1T' Bragg spots in (b) and (c) with the objective aperture marked with blue and orange circles. (f) Overlay of false-colored Dark-field TEM images of the 2H matrix (red) and three different orientations of 1T' grains (green, yellow, and blue). The Dark-field TEM images (d-f) are acquired at the region marked by the yellow dashed square in (a).

2.3.3.2 In-situ electron microscopy measurements for studying the mechanism of anisotropic layer-by-layer phase transition

Next, I perform in situ heating to capture the 2H phase fronts of 1T'-to-2H phase transition with Dark-field TEM images (Figures, 26 a to d). These Dark-field TEM images are formed by selecting the (1-100) 2H Bragg spot with the objective aperture, and therefore, only the 2H regions will show bright intensities in the Dark-field TEM images. Figures 26, a to d show that the 1T'-to-2H phase transition initiates at the existing 2H-1T' interfaces at a temperature as low as 225 °C. This temperature is significantly lower than what has been reported in the literature (1T'-to-2H at 500-600 °C and 2H-to-

1T' at 900-1000 °C) because there is no need for 2H phase nucleation at the 2H-1T' interface.(143, 147) Figure 26e shows a larger field of view with the newly grown 2H regions overlaid on a Dark-field TEM image. It clearly shows that at low temperatures (< 300 °C), 1T'-to-2H phase transition initiates at the 2H-1T' interfaces instead of the 1T'-1T' grain boundaries. The energy barrier for displacive H/1T' phase transition is as high as 0.88 eV/unit formula,(70) which is higher than the thermal energy from annealing at 225 °C (47 meV). The 2H/1T' interface dramatically decreases the energy barrier of 1T'-to-2H phase transition, making it possible to initiate at much lower temperatures. That is to say, the 2H-1T' interfaces act as nuclei with low energy sites and the nearby atoms could locally rearrange into 2H phase at the interfaces, which is analogous to the conventional description of attaching atoms onto nuclei during crystal growth.

Besides the variability and temperature dependence of the propagation rate, another important feature is the anisotropic morphology of the 2H phase. In Figure 26f, I extracted the monolayer 2H phase front I at different time and temperatures to show that the anisotropic growth of 2H phase into the nearby 1T' grain along its b-axis direction ([010] 1T') and remain faceted. This is in contrast to the previously reported isotropic 1T'-to-2H transition, which is an averaged result from large-scale polycrystalline 1T' grains.(81, 150) Note that I observe this preferential, b-axis growth direction for all 1T' orientations. To better understand the anisotropy, I made atomic models of the 2H-1T'

interface as shown in the insets of Figure 26f. Given the 2H matrix and 3 possible 1T' orientations, 2H-1T' interfaces can be classified into 2 major types: 1 Type 1 (interface line is parallel to the b-axis of 1T', mark in green) and type 2 (interface line has an 120° angle with the b-axis of 1T' mark in yellow). The anisotropic growth of 2H phase can be viewed as type 2 interfaces moving into 1T' phase region, while type 1 interfaces are only lengthening themselves. This suggests that the propagation (growth) rate of type 2 interface is much higher than the one for type 1 interface, resulting the belt-shape 2H phase region with mostly type 1 interfaces. This behavior is analogous to the crystal growth process, where the final crystal shape is thermodynamically determined by the surface energy and can be kinetically modified by the relative growth rate of different facets using the kinetic Wulff construction.⁽¹⁵¹⁻¹⁵⁴⁾ In solid-solid phase transition, the surface energy is replaced by the interface energy and the type 2 interface energy is estimated to be 70 meV/ higher than type 1 interface^{A,(96)} making type 1 interfaces more thermodynamically stable. On the other hand, the kinetic aspect is governed by the atomic diffusion and the activation energy barriers. In the atomic resolution HAADF-STEM images of type 1 (Figure 26g) and type 2 (Figure 26f) interfaces, I find more kinks and steps at the type 2 interface, which might act as nucleation sites for the phase transition and greatly reduce the activation energy barrier of the interface. The formation and expansion of atomic kinks also suggest that the 1T'-to-2H phase transition is more diffusive

than displace under our experimental conditions. Unlike crystal growth, where the nucleation and propagation of kinks are driven by the atoms attaching from the environments, the solid-solid phase transition is driven by the diffusion or hopping of the Te atoms at the interface inside the crystal. One distinct example is the morphologies of 2H and 1T'-MoTe₂ islands grown by chemical vapor deposition are usually hexagonal and rectangular,⁽¹¹⁶⁾ which reflect their 3- and 2-fold crystal symmetry. On the contrary, the newly grown 2H phase shows a narrow belt-shape because it is initiated at an interface with two-fold symmetric 1T' phase and being kinetically limited.

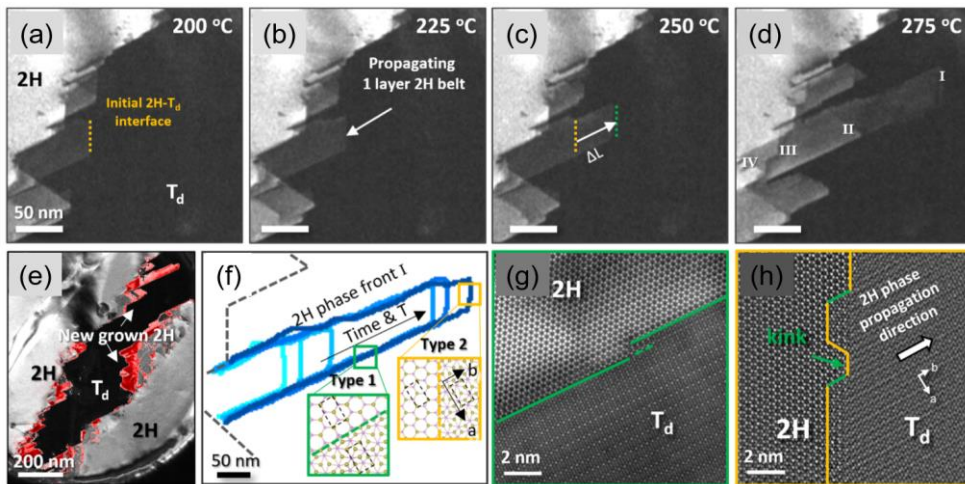


Figure 26. Anisotropic 1T'-to-2H phase transition at low temperatures. (a-d) Dark-field TEM images formed from the (-1100) 2H show the 2H phase front propagating from 200 to 275 °C. (e) Overlay of a low magnification dark-field TEM image with newly grown 2H region marked in red. It shows that the 1T'-to-2H phase transition occurs primarily at 2H-1T' interfaces. (f) The contour plot of 2H phase front propagating anisotropically along the b-axis of

nearby $1T'$ grain in the same region as Fig. 3a-d with increasing temperature. The anisotropy arises from the different interface energy of type 1 and 2 interfaces. HAADF-STEM images of (g) type 1 and (h) type 2 $2H-1T'$ interfaces with kinks indicates a step-flow growth model. The propagation rates of interfaces are limited by its kink formation rate. It is much harder to form kinks on coherent type 1 interface, therefore, the growth of type 1 interface along a-axis ($[100] 1T'$) direction is strongly prohibited.

I notice that the newly grown $2H$ region has multiple phase fronts (I, II, III, and IV) as shown in Figure 27a, indicating a layer-by-layer $1T'$ -to- $2H$ transition mechanism. Although the newly grown $2H$ phase regions inherit the same orientation from the single crystalline $2H$ matrix, each layer undergoes phase transition along the same in-plane direction, suggesting an anisotropic behavior that is not 3-fold symmetric and will be discussed in more details later. Unlike three-dimensional phase transitions in bulk materials, in-plane phase transitions of 2D materials can be precisely measured for each individual layer without the confusion from projection. Figure 27b shows a 4-layer (same thickness as our experiment) MoTe_2 schematic with horizontally staggered $2H$ phase fronts and the resulting Dark-field TEM intensities. The horizontal offset between each $2H-1T'$ interface generates regions with different $2H$ layer thicknesses. To further unveil the phase transition kinetics, I measure the $2H-1T'$ interface positions of each

layer and plot it as a function of accumulated heating time as shown in Figure 27c. The propagation rates are extracted by the slope of the curves and have wide variability between each layer, ranging from 0.07 to 0.4 nm/s at 225 °C and the propagation rates increase at higher temperatures. The temperature dependent growth rate is a typical feature of diffusional phase transition. More specifically, the 1T'-to-2H phase transition can be viewed as local rearrangement of crystal structure induced by diffusion of Te atoms at the 2H-1T' interface. This is in stark contrast to the 2H-to-1T' phase transition that are normally considered as displacive and non-quenchable phase transitions,(123, 155, 156) where the transition is facilitated by collective motion of atoms propagating at the speed of sound (~ 3000 m/s for 1T'-MoTe₂).⁽¹⁵⁷⁾ I find that the 1T'-to-2H transition is well “frozen”, or quenched, with individual heat pulses, which indicates a diffusional type of transition given existing 2H-1T' interfaces. However, a simple diffusional model with a fixed energy barrier cannot explain these inter- and intra-layers variation. For example, both interfaces II (orange) and III (green) exhibit a sudden burst of growth at $t = 300$ sec during the 250 °C heating, while the propagation rate of interface I (blue) slowly reaches a plateau when it gets closer to the edge of the supporting membrane. Both strain and defect densities could locally alter the energy barrier of MoTe₂ phase transitions,⁽¹⁵⁸⁾ while the surface energy between atomic layers (2H, 1T', and Gr encapsulation) may also play a role. These factors need to be considered for more detailed analysis.

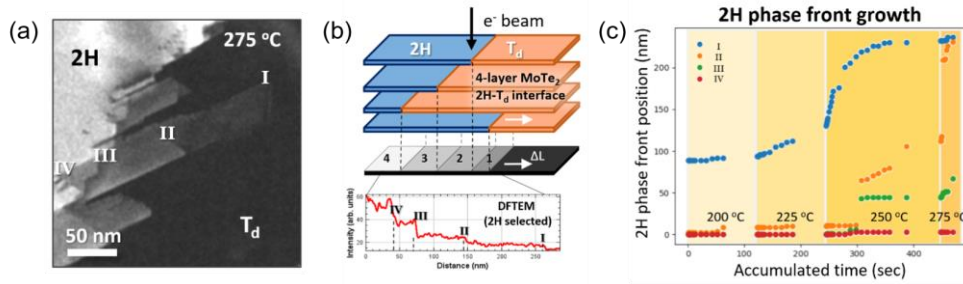


Figure 27. Layer-by-layer phase transition and growth kinetics measurement.

(a) Dark-field TEM image that shows the layer-by-layer phase transition. The 2H-1T' interface of different layers is individually identified by their intensity difference. (b) Schematic of the intensity differences of 4-layer MoTe₂ 2H-1T' interfaces in dark-field TEM. The mono-, bi-, tri-, and quad-layer 2H phase fronts are labeled as I, II, III, and IV respectively. Note that the relative heights (in Z-direction) of each phase front remain unknown due to the projection nature of TEM. (c) Plot of 2H phase front positions of different layers as a function of accumulated heating time.

2.3.4 Conclusions

In conclusion, I demonstrated that graphene encapsulated, few-layer MoTe₂ can be reversibly phase engineered between the semiconducting 2H phase and the semimetallic 1T' phase using laser irradiation and thermal annealing. The laser irradiation technique allows efficient and precise patterning of the 1T' phase, making it promising for coplanar 2D circuitry fabrication. I showed that the 1T'-to-2H phase transition initiates at the 2H-

1T' interfaces at temperatures as low as 225 °C using in situ pulsed heating and dark-field TEM. The dark-field TEM technique also enables independent measurements of 1T'-to-2H phase transition for individual layers. Moreover, I observed anisotropic growth behavior of the 2H phase front, which preferentially propagates along the b-axis of the nearby 1T' grains. These findings shed light on the phase transition mechanism of few-layer MoTe₂ and the techniques are readily available to other phase-change materials.

Chapter 3. Summary

In this thesis, I introduced novel strategies for phase engineering in 2D materials based on hBN encapsulation. The hBN encapsulation improved thermal stability of MoTe₂ in high temperature, which enables to modulate its phase without structural deformation or defect generation. The unique phase transition behaviors of MoTe₂ I studied are summarized in below.

- The phase transition temperature of MoTe₂ increases with decreasing thickness. This is contrary to the behavior of conventional nanoparticles that the phase transition temperature decreases as the particle size decreases. From this, I showed that it is possible to precisely control the phase transition of MoTe₂ by using of dimensionality (thickness and stacking order).
- Layer-controlled annealing and the laser-induced phase transition generate atomically sharp phase boundaries between 2H-T_d(1T') phase, which shows low contact resistance in heterophase junction devices.
- The needed energy for nucleation of 2H phase in T_d matrix is quite high. Fully converted T_d-MoTe₂ crystal without 2H phase did not show phase transition in high temperature. In contrast, the MoTe₂ already having 1T'-2H phase boundary initiates phase transition at the 1T'-2H interfaces at temperature as low as 225 °C. In reversible phase between 2H and 1T', 2H seed decrease the energy barrier.
- The shape of 2H phase is affected by the interface energy between 2H and

1T' phases, which can be explained by the Wulff theorem. The 2H phase grown into 1T' phase has belt-like shape and is oriented to b-axis of 1T' phase, which is different to grown 2H crystal having 3-fold crystal symmetry.

hBN-encapsulation based stable phase transition techniques can be applied to few-layered MoTe₂ in contrast to previous phase transition methods. Since the strength of 2D materials is in the scale-down of device, I expect that the extremely scaled phase changeable device would be demonstrated from our strategies.

References

1. M. Velický, P. S. Toth, From two-dimensional materials to their heterostructures: An electrochemist's perspective. *Appl. Mater. Today* **8**, 68-103 (2017).
2. B. Li *et al.*, Probing van der Waals interactions at two-dimensional heterointerfaces. *Nat. Nanotechnol.* **14**, 567-572 (2019).
3. B. Huang *et al.*, Layer-dependent ferromagnetism in a van der Waals crystal down to the monolayer limit. *Nature* **546**, 270-273 (2017).
4. X.-L. Li *et al.*, Layer-Number Dependent Optical Properties of 2D Materials and Their Application for Thickness Determination. *Adv. Func. Mater.* **27**, 1604468 (2017).
5. R. A. B. Villaos *et al.*, Thickness dependent electronic properties of Pt dichalcogenides. *NPJ 2D Mater. Appl.* **3**, 2 (2019).
6. N. Mounet *et al.*, Two-dimensional materials from high-throughput computational exfoliation of experimentally known compounds. *Nat. Nanotechnol.* **13**, 246-252 (2018).
7. K. Choudhary, I. Kalish, R. Beams, F. Tavazza, High-throughput Identification and Characterization of Two-dimensional Materials using Density functional theory. *Sci. Rep.* **7**, 5179 (2017).
8. S. Manzeli, D. Ovchinnikov, D. Pasquier, O. V. Yazyev, A. Kis, 2D transition metal dichalcogenides. *Nat. Rev. Mater.* **2**, 17033 (2017).
9. F. Shahzad, A. Iqbal, H. Kim, C. M. Koo, 2D Transition Metal Carbides (MXenes): Applications as an Electrically Conducting Material. *Adv. Mater.* **32**, e2002159 (2020).
10. M. C. Lucking *et al.*, Traditional Semiconductors in the Two-Dimensional Limit. *Phys. Rev. Lett.* **120**, 086101 (2018).
11. B. Huang *et al.*, Electrical control of 2D magnetism in bilayer CrI₃. *Nat. Nanotechnol.* **13**, 544-548 (2018).
12. Y. Huang *et al.*, Universal mechanical exfoliation of large-area 2D crystals. *Nat. Commun.* **11**, 2453 (2020).
13. L. Banszerus *et al.*, Ballistic Transport Exceeding 28 μm in CVD Grown Graphene. *Nano Lett.* **16**, 1387-1391 (2016).
14. A. S. Mayorov *et al.*, Micrometer-scale ballistic transport in encapsulated graphene at room temperature. *Nano Lett.* **11**, 2396-2399 (2011).
15. C. Lee, X. Wei, J. W. Kysar, J. Hone, Measurement of the elastic properties and intrinsic strength of monolayer graphene. *Science* **321**, 385-388 (2008).
16. A. A. Balandin, Thermal properties of graphene and nanostructured carbon materials. *Nat. Mater.* **10**, 569-581 (2011).

17. R. R. Nair *et al.*, Fine structure constant defines visual transparency of graphene. *Science* **320**, 1308 (2008).
18. J. S. Bunch *et al.*, Impermeable atomic membranes from graphene sheets. *Nano Lett.* **8**, 2458-2462 (2008).
19. D. Akinwande *et al.*, Graphene and two-dimensional materials for silicon technology. *Nature* **573**, 507-518 (2019).
20. Y. Liu *et al.*, Promises and prospects of two-dimensional transistors. *Nature* **591**, 43-53 (2021).
21. H. Liu, A. T. Neal, P. D. Ye, Channel length scaling of MoS₂ MOSFETs. *ACS Nano* **6**, 8563-8569 (2012).
22. S. B. Desai *et al.*, MoS₂ transistors with 1-nanometer gate lengths. *Science* **354**, 99-102 (2016).
23. A. Srivastava *et al.*, Valley Zeeman effect in elementary optical excitations of monolayer WSe₂. *Nat. Phys.* **11**, 141-147 (2015).
24. T. Tan, X. Jiang, C. Wang, B. Yao, H. Zhang, 2D Material Optoelectronics for Information Functional Device Applications: Status and Challenges. *Adv. Sci.* **7**, 2000058 (2020).
25. J. Yang *et al.*, Robust Excitons and Trions in Monolayer MoTe₂. *ACS Nano* **9**, 6603-6609 (2015).
26. M. Szytniszewski, E. Mostaani, N. D. Drummond, V. I. Fal'ko, Binding energies of trions and biexcitons in two-dimensional semiconductors from diffusion quantum Monte Carlo calculations. *Phys. Rev. B* **95**, 119902 (2017).
27. K. Nassiri Nazif *et al.*, High-specific-power flexible transition metal dichalcogenide solar cells. *Nat. Commun.* **12**, 7034 (2021).
28. D. Akinwande, N. Petrone, J. Hone, Two-dimensional flexible nanoelectronics. *Nat. Commun.* **5**, 5678 (2014).
29. D. Rhodes, S. H. Chae, R. Ribeiro-Palau, J. Hone, Disorder in van der Waals heterostructures of 2D materials. *Nat. Mater.* **18**, 541-549 (2019).
30. L. Wang *et al.*, One-dimensional electrical contact to a two-dimensional material. *Science* **342**, 614-617 (2013).
31. H. R. Gutierrez *et al.*, Extraordinary room-temperature photoluminescence in triangular WS₂ monolayers. *Nano Lett* **13**, 3447-3454 (2013).
32. W. Zhao *et al.*, Evolution of electronic structure in atomically thin sheets of WS₂ and WSe₂. *ACS Nano* **7**, 791-797 (2013).
33. M. Okada *et al.*, Direct chemical vapor deposition growth of WS₂ atomic layers on hexagonal boron nitride. *ACS Nano* **8**, 8273-8277 (2014).
34. G. Grosso *et al.*, Tunable and high-purity room temperature single-photon emission from atomic defects in hexagonal boron nitride. *Nat. Commun.* **8**, 705 (2017).

35. S. B. Song *et al.*, Deep-ultraviolet electroluminescence and photocurrent generation in graphene/hBN/graphene heterostructures. *Nat. Commun.* **12**, 7134 (2021).
36. R. Bourrellier *et al.*, Bright UV Single Photon Emission at Point Defects in h-BN. *Nano Lett* **16**, 4317-4321 (2016).
37. K. S. Novoselov *et al.*, Electric field effect in atomically thin carbon films. *Science* **306**, 666-669 (2004).
38. K. S. Novoselov *et al.*, Two-dimensional atomic crystals. *PNAS* **102**, 10451-10453 (2005).
39. S. B. Desai *et al.*, Gold-Mediated Exfoliation of Ultralarge Optoelectronically-Perfect Monolayers. *Adv. Mater.* **28**, 4053-4058 (2016).
40. H. M. Gramling *et al.*, Spatially Precise Transfer of Patterned Monolayer WS₂ and MoS₂ with Features Larger than 10⁴ μm² Directly from Multilayer Sources. *ACS Appl. Electron. Mater.* **1**, 407-416 (2019).
41. J. Zheng *et al.*, High yield exfoliation of two-dimensional chalcogenides using sodium naphthalenide. *Nat. Commun.* **5**, 2995 (2014).
42. Q. Zhang, L. Mei, X. Cao, Y. Tang, Z. Zeng, Intercalation and exfoliation chemistries of transition metal dichalcogenides. *Journal of Materials Chemistry A* **8**, 15417-15444 (2020).
43. R. Wu *et al.*, van der Waals Epitaxial Growth of Atomically Thin 2D Metals on Dangling-Bond-Free WSe₂ and WS₂. *Adv. Func. Mater.* **29**, 1806611 (2019).
44. C. Kastl *et al.*, Multimodal spectromicroscopy of monolayer WS₂ enabled by ultra-clean van der Waals epitaxy. *2D Mater.* **5**, 045010 (2018).
45. Y. C. Lin *et al.*, Atomically thin heterostructures based on single-layer tungsten diselenide and graphene. *Nano Lett.* **14**, 6936-6941 (2014).
46. S. M. Kim *et al.*, Synthesis of patched or stacked graphene and hBN flakes: a route to hybrid structure discovery. *Nano Lett.* **13**, 933-941 (2013).
47. A. Yan *et al.*, Direct Growth of Single- and Few-Layer MoS₂ on h-BN with Preferred Relative Rotation Angles. *Nano Lett.* **15**, 6324-6331 (2015).
48. S. Behura, P. Nguyen, S. Che, R. Debbarma, V. Berry, Large-Area, Transfer-Free, Oxide-Assisted Synthesis of Hexagonal Boron Nitride Films and Their Heterostructures with MoS₂ and WS₂. *J. Am. Chem. Soc.* **137**, 13060-13065 (2015).
49. M. Zhang *et al.*, Controlled Synthesis of ZrS₂ Monolayer and Few Layers on Hexagonal Boron Nitride. *J. Am. Chem. Soc.* **137**, 7051-7054 (2015).

50. Y. Yu *et al.*, Equally efficient interlayer exciton relaxation and improved absorption in epitaxial and nonepitaxial MoS₂/WS₂ heterostructures. *Nano Lett.* **15**, 486-491 (2015).
51. Y. Gong *et al.*, Vertical and in-plane heterostructures from WS₂/MoS₂ monolayers. *Nat. Mater.* **13**, 1135-1142 (2014).
52. C. Zhang *et al.*, Interlayer couplings, Moire patterns, and 2D electronic superlattices in MoS₂/WSe₂ hetero-bilayers. *Sci. Adv.* **3**, e1601459 (2017).
53. J. Zribi *et al.*, Strong interlayer hybridization in the aligned SnS₂/WSe₂ hetero-bilayer structure. *NPJ 2D Mater. Appl.* **3**, (2019).
54. X. Li *et al.*, Two-dimensional GaSe/MoSe₂ misfit bilayer heterojunctions by van der Waals epitaxy. *Sci. Adv.* **2**, e1501882 (2016).
55. S. M. Eichfeld *et al.*, Highly scalable, atomically thin WSe₂ grown via metal-organic chemical vapor deposition. *ACS Nano* **9**, 2080-2087 (2015).
56. G. Jin *et al.*, Heteroepitaxial van der Waals semiconductor superlattices. *Nat. Nanotechnol.* **16**, 1092-1098 (2021).
57. J. Dong, L. Zhang, X. Dai, F. Ding, The epitaxy of 2D materials growth. *Nat. Commun.* **11**, 5862 (2020).
58. G. H. Ahn *et al.*, Strain-engineered growth of two-dimensional materials. *Nat. Commun.* **8**, 608 (2017).
59. L. Seravalli *et al.*, Gold nanoparticle assisted synthesis of MoS₂ monolayers by chemical vapor deposition. *Nanoscale Adv.* **3**, 4826-4833 (2021).
60. F. Liu, Mechanical exfoliation of large area 2D materials from vdW crystals. *Prog. Surf. Sci.* **96**, 100626 (2021).
61. J. Wang *et al.*, Dual-coupling-guided epitaxial growth of wafer-scale single-crystal WS₂ monolayer on vicinal a-plane sapphire. *Nat. Nanotechnol.* **17**, 33-38 (2022).
62. Z. Cai, B. Liu, X. Zou, H. M. Cheng, Chemical Vapor Deposition Growth and Applications of Two-Dimensional Materials and Their Heterostructures. *Chem. Rev.* **118**, 6091-6133 (2018).
63. Y. Deng *et al.*, MoTe₂: Semiconductor or Semimetal? *ACS Nano*, **15**, 12465–12474 (2021).
64. M. S. Sokolikova, C. Mattevi, Direct synthesis of metastable phases of 2D transition metal dichalcogenides. *Chem. Soc. Rev.* **49**, 3952-3980 (2020).
65. S. Wu *et al.*, Observation of the quantum spin Hall effect up to 100 kelvin in a monolayer crystal. *Science* **359**, 76-79 (2018).
66. Y. Qi *et al.*, Superconductivity in Weyl semimetal candidate MoTe₂. *Nat. Commun.* **7**, 11038 (2016).

67. J. Cui *et al.*, Transport evidence of asymmetric spin-orbit coupling in few-layer superconducting 1T_d-MoTe₂. *Nat. Commun.* **10**, 2044 (2019).
68. Z. Wang *et al.*, MoTe₂: A Type-II Weyl Topological Metal. *Phys. Rev. Lett.* **117**, 056805 (2016).
69. A. Kuc, T. Heine, The electronic structure calculations of two-dimensional transition-metal dichalcogenides in the presence of external electric and magnetic fields. *Chem. Soc. Rev.* **44**, 2603-2614 (2015).
70. K. A. Duerloo, Y. Li, E. J. Reed, Structural phase transitions in two-dimensional Mo- and W-dichalcogenide monolayers. *Nat. Commun.* **5**, 4214 (2014).
71. S. Cho *et al.*, Phase patterning for ohmic homojunction contact in MoTe₂. *Science* **349**, 625-628 (2015).
72. Y. Wang *et al.*, Structural phase transition in monolayer MoTe₂ driven by electrostatic doping. *Nature* **550**, 487-491 (2017).
73. S. Song *et al.*, Room Temperature Semiconductor-Metal Transition of MoTe₂ Thin Films Engineered by Strain. *Nano Lett.* **16**, 188-193 (2016).
74. H. Nan *et al.*, Soft hydrogen plasma induced phase transition in monolayer and few-layer MoTe₂. *Nanotechnology* **30**, 034004 (2019).
75. Y. C. Lin, D. O. Dumcenco, Y. S. Huang, K. Suenaga, Atomic mechanism of the semiconducting-to-metallic phase transition in single-layered MoS₂. *Nat. Nanotechnol.* **9**, 391-396 (2014).
76. F. Zhang *et al.*, Electric-field induced structural transition in vertical MoTe₂- and Mo_{1-x}W_xTe₂-based resistive memories. *Nat. Mater.* **18**, 55-61 (2019).
77. C. Kim *et al.*, High-Electric-Field-Induced Phase Transition and Electrical Breakdown of MoTe₂. *Adv. Electron. Mater.* **6**, 1900964 (2020).
78. H. Xu, J. Zhou, H. Wang, J. Li, Giant Photonic Response of Mexican-Hat Topological Semiconductors for Mid-infrared to Terahertz Applications. *J. Phys. Chem. Lett.* **11**, 6119-6126 (2020).
79. W. Hou *et al.*, Strain-based room-temperature non-volatile MoTe₂ ferroelectric phase change transistor. *Nat. Nanotechnol.* **14**, 668-673 (2019).
80. R. Kappera *et al.*, Phase-engineered low-resistance contacts for ultrathin MoS₂ transistors. *Nat. Mater.* **13**, 1128-1134 (2014).
81. X. Xu *et al.*, Seeded 2D epitaxy of large-area single-crystal films of the van der Waals semiconductor 2H MoTe₂. *Science* **372**, 195-200 (2021).

82. S. H. Tolbert, A. P. Alivisatos, Size Dependence of a First Order Solid-Solid Phase Transition: The Wurtzite to Rock Salt Transformation in CdSe Nanocrystals. *Science* **265**, 373-376 (1994).
83. A. N. Goldstein, C. M. Echer, A. P. Alivisatos, Melting in semiconductor nanocrystals. *Science* **256**, 1425-1427 (1992).
84. J. M. McHale, Surface Energies and Thermodynamic Phase Stability in Nanocrystalline Aluminas. *Science* **277**, 788-791 (1997).
85. J. Park *et al.*, Ultra-large-scale syntheses of monodisperse nanocrystals. *Nat. Mater.* **3**, 891-895 (2004).
86. J. Piella, N. G. Bastús, V. Puntès, Size-Controlled Synthesis of Sub-10-nanometer Citrate-Stabilized Gold Nanoparticles and Related Optical Properties. *Chem. Mater.* **28**, 1066-1075 (2016).
87. K. D. Gilroy *et al.*, Thermal Stability of Metal Nanocrystals: An Investigation of the Surface and Bulk Reconstructions of Pd Concave Icosahedra. *Nano Lett.* **17**, 3655-3661 (2017).
88. G. Kresse, J. Furthmüller, Efficient iterative schemes for ab initio total-energy calculations using a plane-wave basis set. *Phys. Rev. B* **54**, 11169-11186 (1996).
89. G. Kresse, J. Hafner, Ab initio molecular dynamics for liquid metals. *Phys. Rev. B* **47**, 558-561 (1993).
90. I. Hamada, van der Waals density functional made accurate. *Phys. Rev. B* **89**, 121103 (2014).
91. J. Son *et al.*, Atomically precise graphene etch stops for three dimensional integrated systems from two dimensional material heterostructures. *Nat. Commun.* **9**, 3988 (2018).
92. M. Grzeszczyk *et al.*, Raman scattering of few-layers MoTe₂. *2D Mater.* **3**, 025010 (2016).
93. K. Zhang *et al.*, Raman signatures of inversion symmetry breaking and structural phase transition in type-II Weyl semimetal MoTe₂. *Nat. Commun.* **7**, 13552 (2016).
94. Y. Cheon, S. Y. Lim, K. Kim, H. Cheong, Structural Phase Transition and Interlayer Coupling in Few-Layer 1T' and T_d MoTe₂. *ACS Nano*, **15**, 2962-2970 (2021).
95. K. Elibol *et al.*, Atomic Structure of Intrinsic and Electron Irradiation-Induced Defects in MoTe₂. *Chem. Mater.* **30**, 1230-1238 (2018).
96. J. Berry, S. Zhou, J. Han, D. J. Srolovitz, M. P. Haataja, Domain morphology and mechanics of the H/T' transition metal dichalcogenide monolayers. *Phys. Rev. Mater.* **2**, 114002 (2018).
97. K. F. Mak, C. Lee, J. Hone, J. Shan, T. F. Heinz, Atomically thin MoS₂: a new direct-gap semiconductor. *Phys. Rev. Lett.* **105**, 136805 (2010).

98. W. Zhang, Y. Xue, Q. Fu, Z. Cui, S. Wang, Size dependence of phase transition thermodynamics of nanoparticles: A theoretical and experimental study. *Powder Technol.* **308**, 258-265 (2017).
99. M. Wang, Y. Xue, Z. Cui, R. Zhang, Size-Dependent Crystal Transition Thermodynamics of Nano-VO₂ (M). *J. Phys. Chem. C* **122**, 8621-8627 (2018).
100. Z. Cui, H. Duan, Q. Fu, Y. Xue, S. Wang, Universal Size Dependence of Integral Enthalpy and Entropy for Solid–Solid Phase Transitions of Nanocrystals. *J. Phys. Chem. C* **121**, 24831-24836 (2017).
101. D. Li *et al.*, Size-dependent phase transition in methylammonium lead iodide perovskite microplate crystals. *Nat. commun.* **7**, 11330 (2016).
102. L. Liu *et al.*, Size-Dependent Phase Transition in Perovskite Nanocrystals. *J. Phys. Chem. Lett.* **10**, 5451-5457 (2019).
103. J. B. Rivest, L.-K. Fong, P. K. Jain, M. F. Toney, A. P. Alivisatos, Size Dependence of a Temperature-Induced Solid–Solid Phase Transition in Copper(I) Sulfide. *J. Phys. Chem. Lett.* **2**, 2402-2406 (2011).
104. N. Satoh, T. Nakashima, K. Yamamoto, Metastability of anatase: size dependent and irreversible anatase-rutile phase transition in atomic-level precise titania. *Sci. rep.* **3**, 1959 (2013).
105. D. Prabhu *et al.*, Grain size effect on the phase transformation temperature of nanostructured CuFe₂O₄. *J. Appl. Phys.* **109**, 013532 (2011).
106. T. Hu, J. S. Wittenberg, A. M. Lindenberg, Room-temperature stabilization of nanoscale superionic Ag₂Se. *Nanotechnology* **25**, 415705 (2014).
107. T. Y. Kim *et al.*, Electrical Properties of Synthesized Large-Area MoS₂ Field-Effect Transistors Fabricated with Inkjet-Printed Contacts. *ACS Nano* **10**, 2819-2826 (2016).
108. R. Ma *et al.*, MoTe₂ Lateral Homojunction Field-Effect Transistors Fabricated using Flux-Controlled Phase Engineering. *ACS Nano* **13**, 8035-8046 (2019).
109. S. Yang *et al.*, Large-Scale Vertical 1T'/2H MoTe₂ Nanosheet-Based Heterostructures for Low Contact Resistance Transistors. *ACS Appl. Nano Mater.* **3**, 10411-10417 (2020).
110. A. W. Tsen *et al.*, Structure and control of charge density waves in two-dimensional 1T-TaS₂. *PNAS* **112**, 15054-15059 (2015).
111. X. Zhao *et al.*, Healing of Planar Defects in 2D Materials via Grain Boundary Sliding. *Adv. Mater.* **31**, e1900237 (2019).
112. S. Zhu, P. Pochet, H. T. Johnson, Controlling Rotation of Two-Dimensional Material Flakes. *ACS Nano* **13**, 6925-6931 (2019).

113. D. H. Keum *et al.*, Bandgap opening in few-layered monoclinic MoTe₂. *Nat. Phys.* **11**, 482-486 (2015).
114. Y. Cheon, S. Y. Lim, K. Kim, H. Cheong, Structural Phase Transition and Interlayer Coupling in Few-Layer 1T' and T_d MoTe₂. *ACS nano* **15**, 2962-2970 (2021).
115. H. Ryu *et al.*, Anomalous Dimensionality-Driven Phase Transition of MoTe₂ in Van der Waals Heterostructure. *Adv. Func. Mater.*, **31**, 2107376 (2021).
116. J. H. Sung *et al.*, Coplanar semiconductor-metal circuitry defined on few-layer MoTe₂ via polymorphic heteroepitaxy. *Nat. Nanotechnol.* **12**, 1064-1070 (2017).
117. Q. Zhang *et al.*, Simultaneous synthesis and integration of two-dimensional electronic components. *Nat. Electron.* **2**, 164-170 (2019).
118. D.-Y. Lin, H.-P. Hsu, G.-H. Liu, T.-Z. Dai, Y.-T. Shih, Enhanced Photoresponsivity of 2H-MoTe₂ by Inserting 1T-MoTe₂ Interlayer Contact for Photodetector Applications. *Crystals* **11**, 964 (2021).
119. J. C. McGlynn *et al.*, The rapid electrochemical activation of MoTe₂ for the hydrogen evolution reaction. *Nat. commun.* **10**, 4916 (2019).
120. Y. Tan *et al.*, Controllable 2H-to-1T' phase transition in few-layer MoTe₂. *Nanoscale* **10**, 19964-19971 (2018).
121. M. Wang *et al.*, Nonlinear Optical Imaging, Precise Layer Thinning, and Phase Engineering in MoTe₂ with Femtosecond Laser. *ACS nano* **14**, 11169-11177 (2020).
122. K. Sakanashi *et al.*, Investigation of laser-induced-metal phase of MoTe₂ and its contact property via scanning gate microscopy. *Nanotechnology* **31**, 205205 (2020).
123. B. Peng *et al.*, Sub-picosecond photo-induced displacive phase transition in two-dimensional MoTe₂. *NPJ 2D Mater. Appl.* **4**, (2020).
124. Z. Wang, X. Li, G. Zhang, Y. Luo, J. Jiang, Suppressing Electron-Phonon Coupling through Laser-Induced Phase Transition. *ACS Appl. Mater. Interfaces* **9**, 23309-23313 (2017).
125. P. Jiang, X. Qian, R. Yang, L. Lindsay, Anisotropic thermal transport in bulk hexagonal boron nitride. *Phys. Rev. Mater.* **2**, 064005 (2018).
126. D. O. Lindroth, P. Erhart, Thermal transport in van der Waals solids from first-principles calculations. *Phys. Rev. B* **94**, 115205 (2016).
127. M. Omini, A. Sparavigna, Role of grain boundaries as phonon diffraction gratings in the theory of thermal conductivity. *Phys. Rev. B* **61**, 6677-6688 (2000).
128. C. J. Glassbrenner, G. A. Slack, Thermal Conductivity of Silicon and Germanium from 3°K to the Melting Point. *Phys. Rev.* **134**, A1058-A1069 (1964).

129. G. E. Jellison, F. A. Modine, C. W. White, R. F. Wood, R. T. Young, Optical Properties of Heavily Doped Silicon between 1.5 and 4.1 eV. *Phys. Rev. Lett.* **46**, 1414-1417 (1981).
130. A. R. Beal, H. P. Hughes, Kramers-Kronig analysis of the reflectivity spectra of 2H-MoS₂, 2H-MoSe₂ and 2H-MoTe₂. *J. Phys. C Solid State Phys.* **12**, 881-890 (1979).
131. C. Schinke *et al.*, Uncertainty analysis for the coefficient of band-to-band absorption of crystalline silicon. *AIP Advances* **5**, 067168 (2015).
132. P. E. Ciddor, Refractive index of air: new equations for the visible and near infrared. *Appl. Opt.* **35**, 1566-1573 (1996).
133. R. W. Cahn, Binary Alloy Phase Diagrams-Second edition. T. B. Massalski, Editor-in-Chief; H. Okamoto, P. R. Subramanian, L. Kacprzak, Editors. ASM International, Materials Park, Ohio, USA. December 1990. xxii, 3589 pp., 3 vol., hard- back. \$995.00 the set. *Adv. Mater.* **3**, 628-629 (1991).
134. F. Pizzocchero *et al.*, The hot pick-up technique for batch assembly of van der Waals heterostructures. *Nat. commun.* **7**, 11894 (2016).
135. K. J. Tielrooij *et al.*, Out-of-plane heat transfer in van der Waals stacks through electron-hyperbolic phonon coupling. *Nat. Nanotechnol.* **13**, 41-46 (2018).
136. Q. Cai *et al.*, High thermal conductivity of high-quality monolayer boron nitride and its thermal expansion. *Sci. Adv.* **5**, eaav0129 (2019).
137. J. R. Meyer, F. J. Bartoli, M. R. Kruer, Optical heating in semiconductors. *Phys. Rev. B* **21**, 1559-1568 (1980).
138. C. Ruppert, O. B. Aslan, T. F. Heinz, Optical properties and band gap of single- and few-layer MoTe₂ crystals. *Nano Lett.* **14**, 6231-6236 (2014).
139. R. He *et al.*, Dimensionality-driven orthorhombic MoTe₂ at room temperature. *Physical Review B* **97**, 041410 (2018).
140. N. R. Singstock *et al.*, Machine Learning Guided Synthesis of Multinary Chevrel Phase Chalcogenides. *J. Am. Chem. Soc.* **143**, 9113-9122 (2021).
141. A. M. Ionescu, H. Riel, Tunnel field-effect transistors as energy-efficient electronic switches. *Nature* **479**, 329-337 (2011).
142. H.-Y. Chang, W. Zhu, D. Akinwande, On the mobility and contact resistance evaluation for transistors based on MoS₂ or two-dimensional semiconducting atomic crystals. *Appl. Phys. Lett.* **104**, 113504 (2014).
143. X. Xu *et al.*, Scaling-up Atomically Thin Coplanar Semiconductor-Metal Circuitry via Phase Engineered Chemical Assembly. *Nano Lett.* **19**, 6845-6852 (2019).

144. G. H. Ryu, J. Chen, Y. Wen, J. H. Warner, In-Situ Atomic-Scale Dynamics of Thermally Driven Phase Transition of 2D Few-Layered 1T PtSe₂ into Ultrathin 2D Nonlayered PtSe Crystals. *Chem. Mater.* **31**, 9895-9903 (2019).
145. T. Lehnert *et al.*, Electron-Beam-Driven Structure Evolution of Single-Layer MoTe₂ for Quantum Devices. *ACS Appl. Nano Mater.* **2**, 3262-3270 (2019).
146. H. Zhu *et al.*, Defects and Surface Structural Stability of MoTe₂ Under Vacuum Annealing. *ACS Nano* **11**, 11005-11014 (2017).
147. H. Ryu *et al.*, Anomalous Dimensionality-Driven Phase Transition of MoTe₂ in Van der Waals Heterostructure. *Adv. Func. Mater.*, **31**, 2107376 (2021).
148. P. Y. Huang *et al.*, Grains and grain boundaries in single-layer graphene atomic patchwork quilts. *Nature* **469**, 389-392 (2011).
149. A. M. van der Zande *et al.*, Grains and grain boundaries in highly crystalline monolayer molybdenum disulphide. *Nat. Mater.* **12**, 554-561 (2013).
150. X. Xu *et al.*, Millimeter-Scale Single-Crystalline Semiconducting MoTe₂ via Solid-to-Solid Phase Transformation. *J. Am. Chem. Soc.* **141**, 2128-2134 (2019).
151. V. I. Artyukhov, Y. Liu, B. I. Yakobson, Equilibrium at the edge and atomistic mechanisms of graphene growth. *PNAS* **109**, 15136-15140 (2012).
152. T. Ma *et al.*, Edge-controlled growth and kinetics of single-crystal graphene domains by chemical vapor deposition. *PNAS* **110**, 20386-20391 (2013).
153. W. Zhao, F. Ding, Energetics and kinetics of phase transition between a 2H and a 1T MoS₂ monolayer-a theoretical study. *Nanoscale* **9**, 2301-2309 (2017).
154. C.-P. Lin *et al.*, Two-dimensional solid-phase crystallization toward centimeter-scale monocrystalline layered MoTe₂ via two-step annealing. *J. Mater. Chem. C* **9**, 15566-15576 (2021).
155. J. A. Groenink, C. Hakfoort, G. Blasse, The Luminescence of Calcium Molybdate. *Phys. Status Solidi A* **54**, 329-336 (1979).
156. J. Berry, S. Zhou, J. Han, D. J. Srolovitz, M. P. Haataja, Dynamic Phase Engineering of Bendable Transition Metal Dichalcogenide Monolayers. *Nano Lett.* **17**, 2473-2481 (2017).
157. Y. H. Ren, M. Trigo, R. Merlin, V. Adyam, Q. Li, Generation and detection of coherent longitudinal acoustic phonons in the La_{0.67}Sr_{0.33}MnO₃ thin films by femtosecond light pulses. *Appl. Phys. Lett.* **90**, (2007).
158. Q. Tang, Tuning the phase stability of Mo-based TMD monolayers through coupled vacancy defects and lattice strain. *J. Mater. Chem. C* **6**, 9561-9568 (2018).

Abstract in Korean (국문 초록)

전자 소자 응용을 위한 2차원 나노물질 상변이 연구

류희제

공과대학 재료공학부

서울대학교

그래핀, 전이금속 칼코겐화물, 육방정계 질화붕소 등 층상 결정으로부터 분리된 2차원 나노물질은 종류에 따라 금속, 반도체, 절연체 등 다양한 전자기적 성질을 가지며 기존 벌크 전자 소재의 물리적 한계를 극복할 수 있는 차세대 물질로 주목받고 있다.

2차원 나노물질 중 전이금속 칼코겐화물은 다양한 다형체를 가질 수 있으며, 결정 구조에 따른 전자 구조의 변화를 통해 물질의 물리적 성질이 결정된다. 특히, 몰리브데넘 텔루라이드는 다른 전이금속 칼코겐화물에 비해 낮은 상변이 장벽 에너지를 가져 몰리브데넘 텔루라이드를 기반으로 한 2차원 나노물질 상변이 응용 소자 연구가 활발히 진행되고 있다. 여태까지 소개된 상변이 유도인자는 열, 전자 밀도, 기계적 변형, 레이저 등이 있다. 하지만 각 방법에 따른 몰리브데넘 텔루라이드의 결함 발생 및 불균일한 상변이로 인해 2차원 나노물질 고유의 상변이 특성을 분석하는데 한계가 있었다.

본 논문에선 2H 상 몰리브데넘 텔루라이드의 열적, 화학적 안정성을 높이기 위해 육각정계 질화붕소로 몰리브데넘 텔루라이드를 봉지한 반 데르 발스 이종구조를 제작하고, 열을 상변이 인자로 한 몰리브데넘 텔루라이드의 상변이를 소개한다. 육각정계 질화붕소로 봉지된 몰리브데넘 텔루라이드는 공기중에 노출된 상태보다 고온에서 결함이 발행하거나 산화가 일어나지 않고 열역학적으로 안정한 상(T_d)으로 상변이를 나타냈다. 또한 열에너지의 균일한 공급으로

다양한 두께에서 균일한 상변이를 나타냈다.

이를 통해 몰리브데넘 텔루라이드의 층 수에 따른 상변이 임계 온도 변화 경향을 연구할 수 있었으며, 층 수가 감소함에 따라 상변이 임계 온도가 증가함을 확인하였다. 이는 2H, T_d 상의 표면에너지 차이, 수직 방향 압력 및 열에 의해 발생한 전자-정공 쌍이 주요 인자로 작용함에 따른 결과임을 분석하였다. 단위 층 수의 개수에 따라 2차원 나노물질의 상변이를 제어할 수 있었으며, 이를 기반으로 층 수 제어를 통한 국부적인 상 제어를 구현하였다.

또한 열 공급원으로 레이저를 사용하여 육각정계 질화붕소로 봉지된 몰리브데넘 텔루라이드의 상을 국부적으로 제어하였다. 봉지된 구조에 따라 몰리브데넘 텔루라이드의 방열량을 조절함으로써 몰리브데넘 텔루라이드의 온도를 제어할 수 있음을 확인하였으며, 이를 통해 온도에 따른 텔루륨과 몰리브데넘의 원소비가 제어된 상이 발생함을 분석하였다. 레이저를 사용하여 국부적으로 1T' 상을 형성하였으며, 2H-1T' 상이 접합된 동종접합구조 기반 접촉 저항이 매우 낮은 2차원 물질 기반 트랜지스터를 구현할 수 있었다.

마지막으로 2H 결정 내 국부적으로 1T' 상이 형성된 구조에 열에너지를 인가하여 가역적으로 1T' 상에서 2H 상으로 상변이 됨을 확인하였다. 동시 관측 전자현미경을 사용하여 온도에 따른 2H-1T' 상 접합 영역의 구조 변형을 실시간으로 관찰하고, 이를 통해 상변이 전파 메커니즘을 분석하였다. 1T'-2H 상 접합선에서 핵 생성 없이 2H 상이 성장하였으며, 핵 생성 단계가 없음으로 인해 매우 낮은 225도 부근에서 상변이가 발생하였다. 비등방 구조인 1T' 상 내부로 2H 상이 전파함에 따라 상변이는 비등방성을 갖고 전파되었으며, 이는 1T'-2H 상 접합선의 계면 에너지 차이에 기인하였다.

몰리브데넘 다이텔루라이드의 두께와 온도에 따른 상변이 제어 기술은 2차원 나노물질의 동종접합 기반 전자소자 응용 가능성을 보여주었으며, 특히 가역적 상변이 현상은 메모리 소자에 적용될 수

있음을 보여주었다.

주제어: 2차원 나노물질, 폴리브테덤 텔루라이드, 육방정계 질화붕소, 반데르 발스 이종구조, 상변이, 2차원 전자소자'

학번: 2019-266834